RESEARCH ARTICLE
SPACE PHYSICS

Earth and Planetary Physics
8: 479–496, 2024
doi: 10.26464/epp2024026

Semiannual oscillation, annual oscillation, quasibiennial oscillation, and solar cycle variation of the OH airglow emission in the mesopause region

Sheng-Yang Gu[1]*, Dong Wang[1], YuSong Qin[1], Liang Tang[2], YaFei Wei[1], and XianKang Dou[1]

[1]Electronic Information School, Wuhan University, Wuhan 430072, China;

[2]School of Optoelectronic Engineering, Chongqing University of Posts and Telecommunications, Chongqing 400065, China

Key Points:

- We studied the semiannual oscillation, annual oscillation, quasibiennial oscillation, and solar cycle variations of the OH airglow by calculating its vertically integrated emission rate, centroid altitude, peak emission rate, and peak height.
- The amplitude and phase variations of the semiannual oscillation and quasibiennial oscillation in OH in the equatorial region are strongly correlated with the migrating diurnal tide (DW1) amplitude variations and the vertical transport of atomic oxygen.
- Solar activity modulates OH radiation mainly through chemical rather than dynamic processes.

Citation: Gu, S.-Y., Wang, D., Qin, Y. S., Tang, L., Wei, Y. F., and Dou, X. K. (2024). Semiannual oscillation, annual oscillation, quasibiennial oscillation, and solar cycle variation of the OH airglow emission in the mesopause region. *Earth Planet. Phys.*, *8*(3), 479–496. http://doi.org/10.26464/epp2024026

Abstract: The vertically integrated emission rate, centroid altitude, peak emission rate, and peak height of the hydroxyl (OH) airglow were calculated from Thermosphere Ionosphere Mesosphere Energetics and Dynamics (TIMED)/Sounding of the Atmosphere using Broadband Emission Radiometry (SABER) observations to study the seasonal and interannual variations in the intensity and location of the OH emission. The emission rate is inversely proportional to the height of the emission, with the semiannual oscillation dominating at low latitudes and the annual oscillation dominating at higher latitudes. The OH emission is modulated by the quasibiennial oscillation at the equator, and the quasibiennial oscillation signal is weak at other latitudes. We represented the vertical transport of atomic oxygen by using atomic oxygen concentrations obtained from a global atmospheric model, the Specified Dynamics Whole Atmosphere Community Climate Model with thermosphere and ionosphere eXtension simulations. Compared with the amplitudes of the migrating diurnal tide (DW1) calculated from temperature data observed by TIMED/SABER, we found that both the vertical transport of atomic oxygen and DW1 amplitudes in the equatorial region exhibit semiannual oscillation and quasibiennial oscillation, which have a strong correlation with the variations in the amplitude and phase of semiannual oscillation and quasibiennial oscillation in OH emission. It is likely that the DW1 affects the vertical transport of atomic oxygen that is involved in the reaction to produce O_3, thus affecting the OH emission. We analyzed the relationship between OH emission and solar activity by using the solar radio flux at 10.7 cm as a proxy for solar activity. The results showed that the OH emission is well correlated with solar activity, and the modulation of OH emission by solar activity has a significant latitudinal variation. The small correlation between emission height and solar activity indicates that solar activity modulates OH emission mainly through chemical rather than dynamic processes.

Keywords: OH airglow; semiannual oscillation; quasibiennial oscillation; solar activity; diurnal tide

1. Introduction

The energy required for airglow emission is supplied by solar electromagnetic radiation. Through direct and indirect action, solar radiation excites atoms, molecules, and ions in the upper atmosphere to higher energy states and activates particles to emit photons when they transition from high energy states to lower energy states (i.e., generating airglow). The hydroxyl (OH) vibration-rotation band is generated by the radiation transition between the vibrational energy levels of the ground state of the OH electron. The source of its production mainly comes from the chemical reaction between hydrogen atoms and ozone:

$$O_3 + H \xrightarrow{k1} OH\,(v \le 9) + O_2. \quad (1)$$

The temporal and spatial distribution of airglow is modulated by various atmospheric dynamic processes, such as atmospheric gravity, tidal, and planetary waves. As radiation from the atmosphere itself, the airglow carries a wealth of information about the middle and upper atmosphere and can be used as a medium for the study of various dynamic and photochemical processes in the middle and upper atmosphere. The emission rate and the emission

Correspondence to: S. Y. Gu, gushengyang@whu.edu.cn
Received 02 JAN 2023; Accepted 02 APR 2024.
First Published online 07 MAY 2024.

height of the OH airglow indicate atmospheric changes. It is conceivable that because the O_3 + H reaction is an important heating source in the mesopause region, the variation in intensity and location of the OH emission means that the energetics of the mesopause are being altered significantly. The important goal of this study is to investigate how the OH emission rate and emission intensity vary, as well as to probe the role that temperature, chemistry, and dynamics play in this.

The changing characteristics of the OH airglow have been studied for a long time. Whether using ground-based observations or satellite remote sensing observations, many studies have been conducted on the seasonal variation in OH airglow intensity. Abreu and Yee (1989) analyzed the nighttime patterns of OH(8-3) airglow measured on the Atmosphere Explorer-E satellite and found that the diurnal variation in OH emissions is a function of latitude and season. They also observed a strong semiannual oscillation with a maximum near the equator. Takahashi et al. (1995) measured the OH airglow by using a ground-based multichannel airglow photometer near Fortaleza, Brazil (3.9°S, 38.4°W), and found that the OH airglow intensity shows semiannual oscillation, with maxima at the equinoxes and minima at the solstices. Zaragoza et al. (2001) used OH airglow data measured by the Improved Stratospheric and Mesospheric Sounder (ISAMS) instrument on the Upper Atmosphere Research Satellite (UARS) and found significant semiannual variations at low latitudes, especially at equatorial regions, and annual variations at higher latitudes. López-González et al. (2004) analyzed more than 3 years of OH(6-2) airglow observations at the Sierra Nevada Observatory in Granada, Spain (37.06°N, 3.38°W), and found that the amplitudes of annual and semiannual variations in OH emission rates were comparable. Buriti et al. (2004) analyzed the intensity data of OH(6-2) airglow radiation observed at equatorial stations from 1998 to 2001 and found a half-yearly cycle of variation. The maximum value of airglow intensity appears at the equinoxes, and the minimum value appears at the solstices. The authors suggested that atmospheric tidal oscillations play an important role in the observed semiannual oscillation. Taylor et al. (2005) found semiannual oscillations in mesospheric temperature and the intensity of the OH(6-2) and O_2(0-1) airglow by using 25 months of Maui, Hawaii (20.8°N, 156.2°W), Mesospheric Temperature Mapper observations and that the spring perturbation is also greater than that in autumn. Shepherd et al. (2006) analyzed the seasonal variations of O(^{1}S) green line and OH(8-3) nightglow from data obtained by the Wind Imaging Interferometer (WINDII) on the UARS and found a strong semiannual variation dominating at the equator, which is thought to be driven by the semiannual variation in diurnal tidal amplitudes, and that tidal modulation is also present in the annual variation at mid-latitudes. Gao H et al. (2010) used the OH airglow emission data from TIMED/SABER observations to analyze which oscillations dominate the OH airglow emission and the distribution of these oscillations. Strong semiannual oscillations in the OH airglow emission in the equatorial region have been observed by using different observational methods. The maximum value of OH airglow emission in the equatorial region occurs at the equinox, and the minimum value occurs at the solstice. With increasing latitude, the annual oscillation dominates at higher latitudes.

Great progress has been made in understanding not only the seasonal variation but also the long-term variation in OH airglow emission. Wiens and Weill (1973) analyzed the diurnal, annual, and solar cycle variations of the OH airglow by studying OH airglow intensity data observed by filter photometers in the tropics and at latitude stations in the northern and southern temperate zones. They found that the diurnal variation pattern is a function of latitude and season and that the OH airglow intensity is influenced by solar activity. Batista et al. (1994) found a positive correlation between the OH(9-4) airglow intensity obtained in Brazil (23°S, 45°W) from 1977 to 1986 and the $F_{10.7}$ index (solar radio flux at 10.7 cm) by analyzing the relationship between this intensity and the intensity of solar activity. Liu G and Shepherd (2006) analyzed the relationship between OH airglow emission and solar radiation by using the WINDII observation data from 1991 to 1997 and pointed out that the OH airglow emission is dependent on solar radiation. Baker et al. (2007) found that for several years, the experimental data from SABER exhibited equatorial enhancements of the nighttime mesospheric OH airglow layer consistent with the high average diurnal solar flux. Pertsev and Perminov (2008) analyzed the response of OH(6-2) airglow to solar activity by using observations from the Zvenigorod Observatory in Moscow (56°N, 37°E) and found that the response of emission intensity to the variation in $F_{10.7}$ solar radio flux was 30%–40%/100 solar flux units (sfu), with a more significant response in winter compared with summer. Reid et al. (2014) analyzed OH(8-3) airglow data obtained from filter photometer measurements near Adelaide, Australia. The results showed that the OH airglow intensity is related to solar activity. Many studies have shown that the intensity of OH airglow is closely related to solar activity but that the emission height of OH airglow shows a different response. von Savigny (2015) analyzed the vertical volume emission rate of OH(3-1) airglow observed by the Scanning Imaging Absorption Spectrometer for Atmospheric Cartography (SCIAMACHY) on the Envisat satellite and found no significant solar cycle signature for the OH emission height. Teiser and von Savigny (2017) analyzed the variability of emission rate and centroid emission altitude in the OH(3-1) and OH(6-2) Meinel bands based on Earth's nighttime luminous data measured by the SCIAMACHY instrument from August 2002 to April 2012. They found that at low latitudes, the dominant sources of variation for both the OH emission rate and altitude were semiannual variations. In addition, they found an 11-year solar cycle signature in the emission rate and centroid emission altitude. Gao H et al. (2016) used the airglow data observed by SABER to analyze the response of 2.0 μm and 1.6 μm OH airglow to solar radiation. They found that the intensity and peak emission rate of the four airglow emissions were strongly correlated with solar radiation but that the response of NO and the 1.6 and 2.0 μm OH airglow peak heights to solar radiation was not significant. They also pointed out that the response of airglow emission to solar radiation varies with latitude.

Numerical models are often analyzed in conjunction with observational data to study the relationship between OH airglow radiation changes and dynamic processes and solar activity changes. Yee et al. (1997) analyzed 3 days of observations (including the O(^{1}S) green line, O_2(0-1) atmospheric band, and OH Meinel band luminous emission) from the High Resolution Doppler Imager

(HRDI) on the UARS near the September equinox of 1993 and simulations from the Thermosphere-Ionosphere-Mesosphere-Electrodynamics General Circulation Model (TIME-GCM). The authors showed that the vertical motion, driven mainly by tides, changes the atomic oxygen profile, leading to changes in the observed peak height and brightness of the airglow. The upward motion reduces the atomic oxygen concentration at the top height of the mesosphere, thus reducing the OH airglow intensity. Marsh et al. (2006) examined the variations in OH Meinel airglow by comparing SABER measurements of OH airglow with predictions from a three-dimensional (3D) chemical dynamic model. They found that migrating diurnal tides have a considerable influence on diurnal and seasonal variations at low latitudes, whereas at high latitudes, the annual variations in emissions are mainly due to the transport of oxygen by the seasonally reversed mean circulation. Huang TY (2016) used a two-dimensional (2D), time-dependent, nonlinear OH Chemistry-Dynamics (OHCD) model and a Multiple Airglow Chemistry-Dynamics (MACD) model to simulate OH airglow and O airglow to study the effects of CO_2 gas concentration variation and solar cycle variation on airglow intensity and the volume emission rate. The results showed that the effect of solar cycle variation on airglow variation was greater than the effect of CO_2 gas concentration variation on airglow variation.

One of the most important applications of airglow emission is the acquisition of atmospheric temperature in the mesopause region. Especially in the early stages when satellite observations were not available, the observation of airglow emission in ground-based experiments was an effective tool for sustained observation of the temperature in the mesopause region. As described by von Savigny (2015), the atmospheric temperature retrieved in ground-based experiments was, in fact, the temperature weighted by the airglow emission layer. As a result, it is often assumed that the observed temperature variations are solely due to temperature variations at a certain altitude. In fact, the height of the nightglow emission varies with time, and a downward shift of the OH(3-1) nightglow profile by 0.5 km can cause the emission rate weighted temperature to increase by 0.65 K (von Savigny et al., 2012; von Savigny, 2015). A clear seasonal variation exists in OH airglow peak heights, and the magnitude varies with latitude. This can result in uncertainty in the seasonal variations in temperatures derived on the basis of the assumption that the OH emission altitude is a constant. To check the reasonableness of the assumption in the study of temperature variations from ground-based nightglow observations, it is necessary to study the seasonal variations in OH airglow peak heights and the response to solar radiation.

Previous work on OH airglow characterization has focused more on the variability of OH airglow intensity, and in this article, we have chosen to use other quantities, such as peak emission rates and peak heights, that are also of value to the surface OH population. Understanding the variability in OH emission heights is important for using OH emission measurements to retrieve temperature in the mesopause region. In addition to analyzing peak emission rates, vertically integrated emission rates should be analyzed. The latter are much more important for many ground-based observers. Anomalous variations are present in the 2015–2016 quasibiennial oscillation, and we were also concerned about anomalous variations present in the OH airglow emission.

Using the OH volume emission rate data from SABER observations, we calculated the vertically integrated emission rate, given that studying its variation is important to many ground-based observers. The centroid altitude (i.e., the altitude weighted by the emission rate profile) can be used to describe the location of OH emission. In addition, the peak emission rate and peak height are good quantities for describing the intensity and location of OH emission. Through the vertically integrated emission rate, centroid altitude, peak emission rate, and peak height, these four quantities visualize the overall intensity and location of OH emission as well as the maximum emission and the corresponding height. Studying the seasonal and interannual variability of OH emission in the mesosphere–lower thermosphere (MLT) region, analyzing the causes of the variability, and comparing the roles of temperature, chemistry, and dynamics in the observed variability in OH emission are important for understanding the energetic, chemical, dynamic, and transport processes in the MLT region.

In this work, we analyzed the seasonal and interannual variability of OH emission intensity and location by using OH airglow data from 2002 to 2022 observed by SABER. In Section 2, we describe the data and analysis methods. In Section 3, we obtain the periodic features present in the OH emission by using Lomb–Scargle periodograms, and we calculate the diurnal tidal amplitude variations by using temperature data from SABER observations. The main periodic features analyzed include the semiannual oscillation, annual oscillation, quasibiennial oscillation, and solar activity cycles. A summary is given in Section 4.

2. Data and Methods

2.1 TIMED/SABER

The SABER instrument is one of four instruments on the National Aeronautics and Space Administration's (NASA's) TIMED satellite. The SABER makes global measurements of the atmosphere by using a broadband limb-scanning infrared radiometer that measures not only the volume mixing ratios of O_3, CO_2, H_2O, O, and H, but also the volume emission rates for NO, OH, and O_2. The wavelengths of the OH airglow emission centers measured by SABER are 2.0 and 1.6 μm. The 2.0 μm channel measures the radiation from the OH(9-7) and OH(8-6) bands, whereas the 1.6 μm channel measures the radiation from the OH(5-3) and OH(4-2) bands and part of the OH(3-1) band (Russell et al., 1999).

We used version 2.07 1.6 μm OH volume emission rate data, volume mixing ratio data for O_3 and H, and temperature data from January 25, 2002, to December 14, 2019. Data from December 15, 2019, to December 31, 2022, used the new version, v2.08. Limb profiles were taken from a circular orbit at 625 km inclined at 74° to the equator and covered a latitudinal range from 54°S to 82°N or 82°S to 54°N, depending on the phase of the yaw cycle (Russell et al., 1999). To ensure data continuity at high latitudes and avoid inconsistent analysis caused by missing measurements at high latitudes, we chose to analyze OH airglow emission in the latitudinal range of 52.5°N–52.5°S. Before analyzing the long-term variation in OH airglow, we needed to extract these data from the altitude profiles of OH airglow volume emission rates. The altitude range of OH in SABER Level 2A Routine Products is 80–100 km (Russell et al., 1999), so we used the Fourier fourth-order fitting

method for the observation points near this range:

$$V(z) = a_0 + \sum_{i=1}^{4} [a_i \cos(i \times \omega \times z) + b_i \sin(i \times \omega \times z)], \quad (2)$$

where z is the height, $i \times \omega$ is the angular velocity of the rotation vector, and V is the OH airglow emission rate, resulting in the peak OH airglow emission rate and peak height, which are hereafter expressed as the peak emission rate V_{max} and peak height h_{max}, respectively. This method was used to carry out the study of seasonal and interannual variations in peak OH airglow emission. Figure 1 shows an example of the observed and fitted height profile of the OH airglow volume emission at 30°S on December 1, 2003. The dashed lines in the figure point to the peak emission rate (V_{max}) and peak height (h_{max}), respectively.

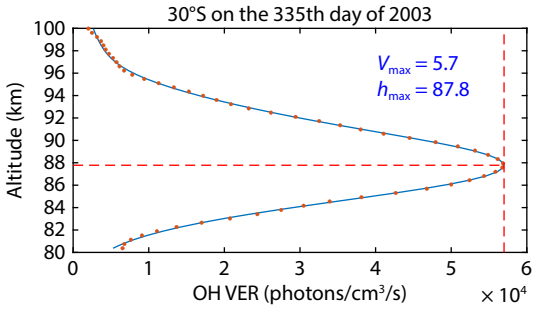

Figure 1. Observations (points) and fitted curves (solid lines) of the OH airglow emission rate on December 1, 2003, where the units of the emission rate and height are photons per cubic centimeter per second and kilometers, respectively. VER, volume emission rate.

To compare this profile with ground-based observations, we calculated the integrated volume emission rate I and the centroid emission altitude Z between 80 and 100 km. The vertically integrated emission rate is given by

$$I = \int_{z_1}^{z_2} V(z)\,\mathrm{d}z, \quad (3)$$

where $V(z)$ is the OH volume emission rate. Altitude Z is determined by weighting z with the volume emission rate profile of OH:

$$Z = \frac{\int_{z_1}^{z_2} z \times V(z)\,\mathrm{d}z}{\int_{z_1}^{z_2} V(z)\,\mathrm{d}z}, \quad (4)$$

where z_1 = 80 km and z_2 = 100 km. These parameters were investigated to describe the variations in the OH volume emission rate profiles.

The SABER retrievals gave global temperature profiles from approximately 20 km to above 110 km. In this work, we chose a 61-day sliding temporal window with a step of 1 day to extract the tide and its temporal variations. For the temperature data from the TIMED/SABER observations, we used the 2D least-squares fitting method (Wu DL et al., 1995):

$$y = A\cos\left[2\pi\left(\frac{t}{T} - s\lambda\right)\right] + B\sin\left[2\pi\left(\frac{t}{T} - s\lambda\right)\right] + C, \quad (5)$$

where t is the observational time in hours, T represents the period of the tides in hours, s is the zonal wavenumber of the tides (where negative corresponds to westward), and λ is the longitude (in radian) of the observation normalized by 2π. During the analysis, the periods varied from 2 to 36 h with steps of 1 h to determine the spectra of the observation and the amplitudes of the tides. The coefficients included A, B, and C, where C represents the background value. The amplitudes of the tides were expressed as

$$R^2(T, s) = A^2(T, s) + B^2(T, s). \quad (6)$$

2.2 Space Physics Data Facility

The Space Physics Data Facility is NASA's active and permanent archive for nonsolar heliophysics data (solar data are archived at the Solar Data Analysis Center). The solar radio flux at 10.7 cm (2800 MHz) is an excellent indicator of solar activity. Often called the $F_{10.7}$ index, it is one of the longest running records of solar activity. We chose to use the $F_{10.7}$ index provided by the Space Physics Data Facility's OMNIWeb to represent solar activity. The time range of the data was 2002–2022, with daily averages.

2.3 MERRA-2

The second Modern-Era Retrospective analysis for Research and Applications (MERRA-2) is a NASA atmospheric reanalysis using version 5.12.4 of the Goddard Earth Observing System Model, Version 5 (GEOS-5), which enables the use of newer microwave sounders and hyperspectral infrared radiance instruments, as well as other data types. Unlike MERRA, all data sets for MERRA-2 are available on the same horizontal grid. This grid has 576 points in the longitudinal direction and 361 points in the latitudinal direction, corresponding to a resolution of 0.625° × 0.5°. The longitudinal resolution of the data is changed from 0.667° in MERRA and the latitudinal resolution remains the same (0.5°). The MERRA-2 wind field data contain up to 80 km of zonal wind data with a temporal resolution of 3 h. We chose to characterize the equatorial stratospheric quasibiennial oscillation by using zonal winds up to a pressure level of 11 hPa in the Singapore region (0.625°N, 103.125°E).

2.4 SD-WACCM-X

The SD-WACCM-X is a Specified Dynamics mode of the Whole Atmosphere Community Climate Model (WACCM) with thermosphere and ionosphere eXtension (WACCM-X), which is a comprehensive atmospheric coupled numerical model developed by the National Center for Atmospheric Research (NCAR). The WACCM-X uses the NCAR Community Earth System Model (CESM) as a common numerical framework and spans a range of altitudes from the Earth's surface to the upper atmosphere, with a top boundary height ranging from 500 to 700 km. In addition to the atmospheric component, components are provided for oceans, land, sea ice, and so on. In this work, we used O concentrations from the SD-WACCM-X model for 2002–2019.

3. Results and Discussion

3.1 Lomb-Scargle Periodograms

The OH airglow emission data for each day were first binned in 1 h and 5° latitude ranges. After averaging these data, we obtained the zonal mean I, Z, V_{max}, and h_{max} of the OH airglow emission at 21 latitudes from 52.5°S to 52.5°N at 24 local times. Zonal averaging

largely removes the variability attributable to gravity and planetary wave perturbations, but it cannot isolate the effects of tides, which are superimposed on the background mean values. In fact, in each day, there are data in only one or two local time bins because the orbital period of the TIMED satellite is approximately 1.6 h (~15 orbits/day), and it takes ~60 days to complete a full 24-h coverage of local time. Therefore, at a specific latitude and altitude, the data in a 60-day window were combined to produce the full 24 h of local time coverage, and we defined them as the data on the central day of the window. Repeating the method above and offsetting the window by 1 day resulted in an overlap analysis, as shown in Figure 2. The time range of the OH data used was from January 25, 2002, to December 31, 2022. However, when calculating a certain time, data for some time before that time are needed, so the time range in Figure 2 is from 2003 to 2021.

Figure 3 shows the Lomb–Scargle periodograms of four OH airglow parameters at five latitudes, 50°N, 25°N, 0°S, 25°S, and 50°S, for the years 2003–2014. The range of time chosen was from 2003 to 2014, and the oscillations were more pronounced near the period of 834 days. The range of time chosen was from 2003 to 2021, and the oscillations were very weak and negligible around the period of 834 days. The reason for this situation is analyzed in Section 3.4. The time series for all four parameters show periods of 121, 183, 365, and 834 days with a confidence level greater than 99%. Comparing the different latitudes, we found that oscillations with periods of 183 and 834 days dominate at low latitudes and that oscillations with periods of 365 days dominate at mid-latitudes. Reid et al. (2014) analyzed 15 years (1995–2010) of atomic oxygen (OI) 558 nm and OH(8-3) 730 nm nightglow emission intensities from heights near 96 km and 87 km, respectively, measured by using filter photometers at the Buckland Park Field Station (34.6°S, 138.6°E) near Adelaide, Australia. They found oscillations with periods of 183, 365, and 770 days in the time series of OH airglow intensity. This finding is in general agreement with our results.

3.2 The Migrating Diurnal Tide

Solar atmospheric tides are persistent global-scale waves with periods that are harmonics of a solar day. The migrating diurnal tide is a 24-h westward-propagating zonal wavenumber 1 (i.e., $s = -1$) wave that is Sun synchronous. Like other migrating solar tides, this wave is primarily excited by the absorption of solar radiation throughout the atmosphere. So-called nonmigrating solar diurnal tidal components are $s \neq -1$ global perturbations with periods of 24 h, where s represents the zonal wavenumber. Thus, these waves can be standing (i.e., $s = 0$), or they can propagate either eastward (i.e., $s > 0$) or westward (i.e., $s < 0$). The seasonal cycle of the diurnal tide in the mesopause region and its strong semiannual component are well known.

The temperature wavenumber–period spectrum at 85 km and the equator during days 152–212 of 2015 is exhibited in Figure 4a. Enhanced wave activities are shown to be westward propagating with zonal wavenumber 1 and a period of 24 h, which can be identified as the migrating diurnal tide (DW1). The spatial structure of the DW1 from the SABER temperature is shown in Figure 4b. Two large amplitudes occur near the equator at altitudes of approximately 85 km and 95 km, reaching 13 K and 15 K, respectively. The temporal structure of the DW1 amplitude from 2003 to 2021 is presented in Figure 4c. Strong semiannual oscillations can be observed between 80 and 90 km. We followed the same treatment for the DW1 amplitude at 85 km as for the OH airglow, and the calculated latitude–time distribution is shown in Figure 4d. The DW1 amplitude at 85 km was chosen for study because the height of the peak altitude is approximately 85 km.

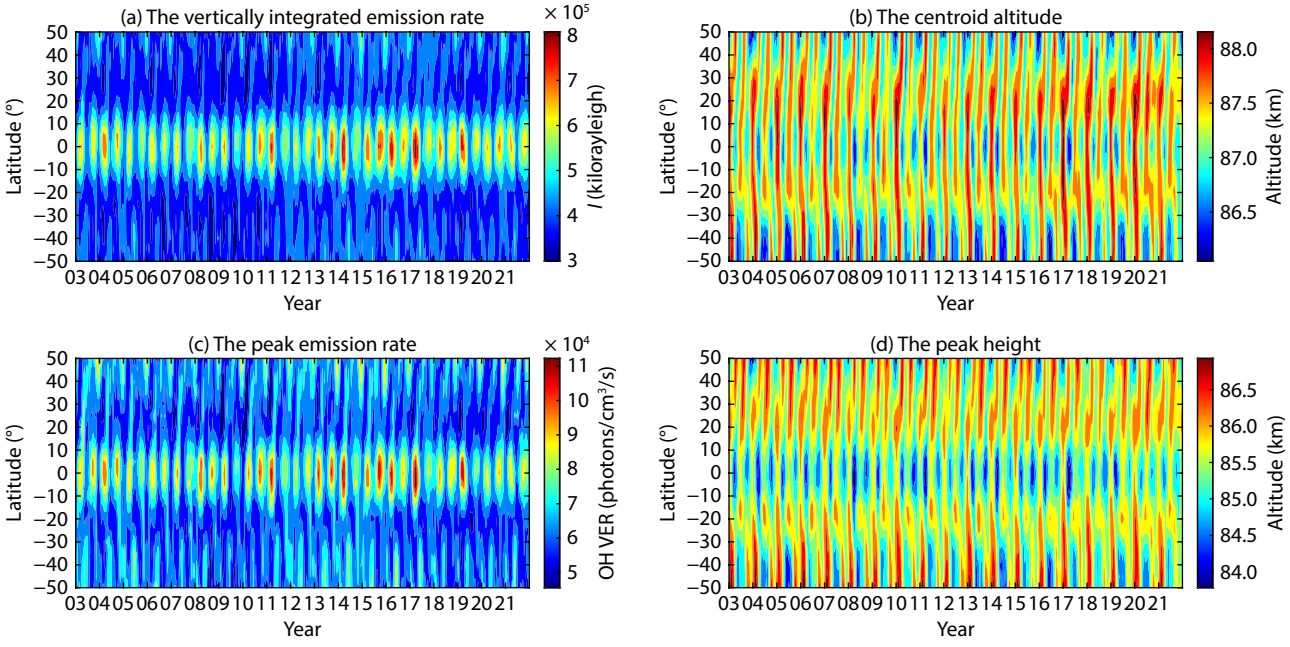

Figure 2. (a) Latitude–time distribution of the vertically integrated emission rate I. (b) Latitude–time distribution of the centroid altitude Z. (c) Latitude–time distribution of the peak emission rate V_{max}. (d) Latitude–time distribution of the peak height h_{max}. The period starts from January 1, 2003, and ends on December 31, 2021. VER, volume emission rate.

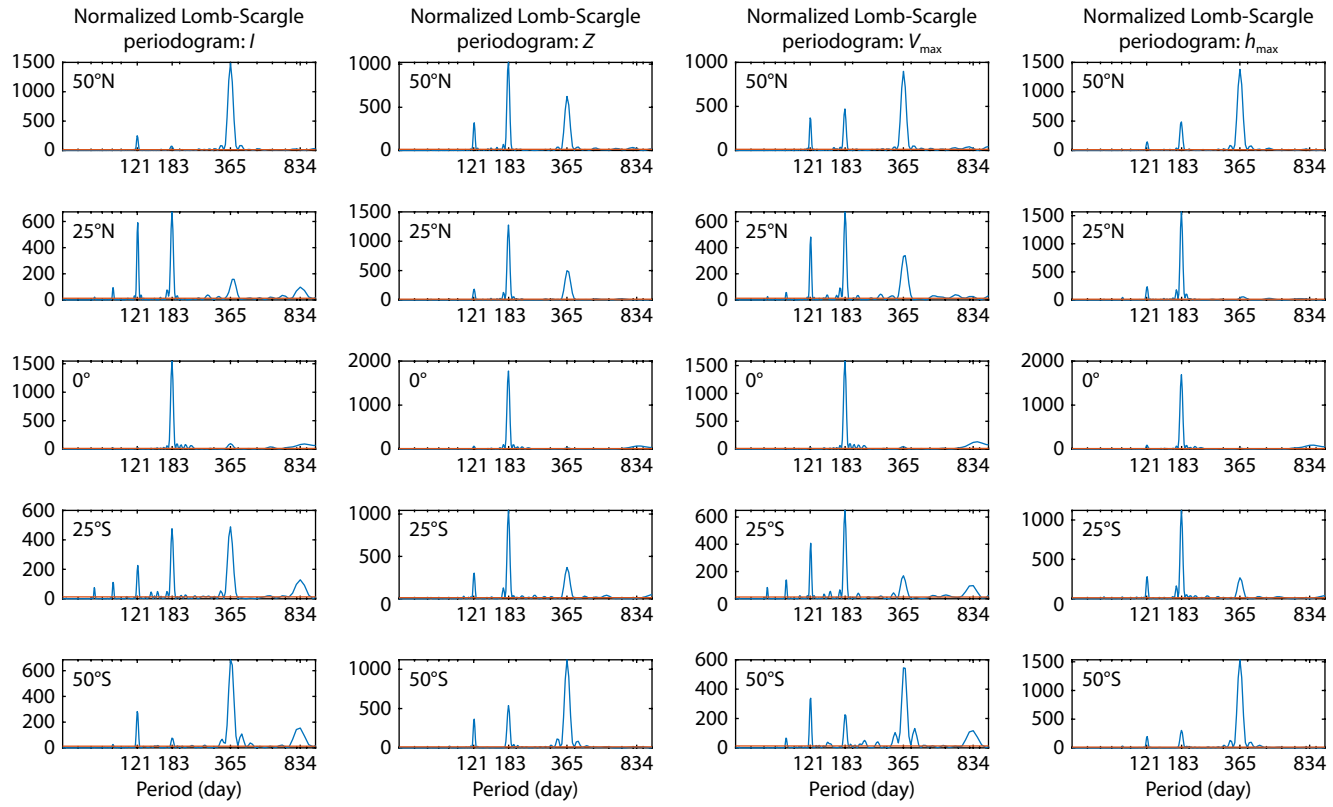

Figure 3. Lomb–Scargle periodograms calculated from the vertically integrated emission rate (*I*), the centroid altitude (*Z*), the peak emission rate (V_{max}), and the peak height (h_{max}) at five latitudes. The red lines denote the 99% confidence levels.

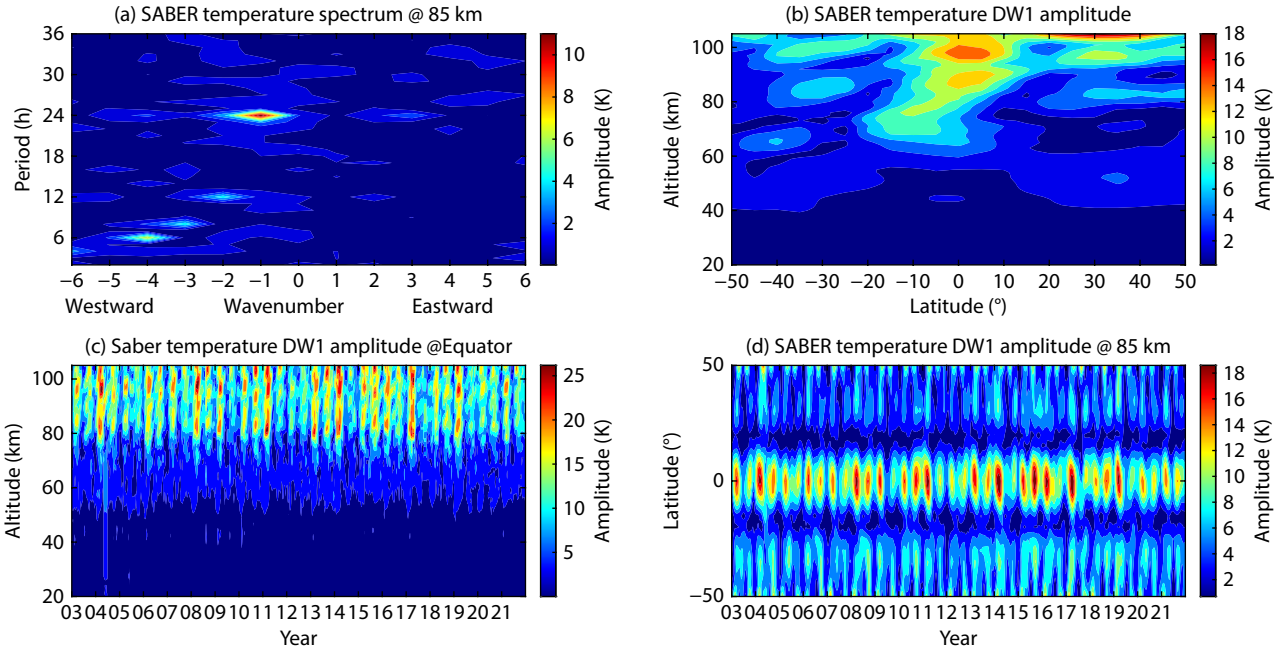

Figure 4. (a) The wavenumber–period spectrum of SABER temperature observations at 85 km and the equator during days 152–212 of 2015. (b) The spatial structure of the DW1 amplitude on day 180 of 2015. (c) The temporal structure of the DW1 amplitude from 2003 to 2021. (d) Latitude–time distribution of the DW1 amplitude.

3.3 Annual and Semiannual Oscillation

To facilitate the study of annual and semiannual oscillation of airglow radiation, airglow radiation data for 19 years, from 2003 to 2021, were averaged by superimposing them. A superimposed year was obtained that could be used to represent a multiyear average of OH airglow. Figure 5a shows the vertically integrated emission rate after multiyear averaging, and a clear semiannual oscillation can be seen in the equatorial region. The maximum

value is at the equinox, and the minimum value is at the solstice. The extreme value at the March equinox is larger than that at the September equinox, which is consistent with previous studies (Mulligan et al., 1995; Takahashi et al., 1995; Buriti et al., 2004). Figures 6b–6d are treated in the same way as Figure 5a, corresponding to one superimposed year of the centroid altitude, peak emission rate, and peak height, respectively.

Figure 5d shows the OH airglow peak height after multiyear averaging. The peak height has the same semiannual oscillation

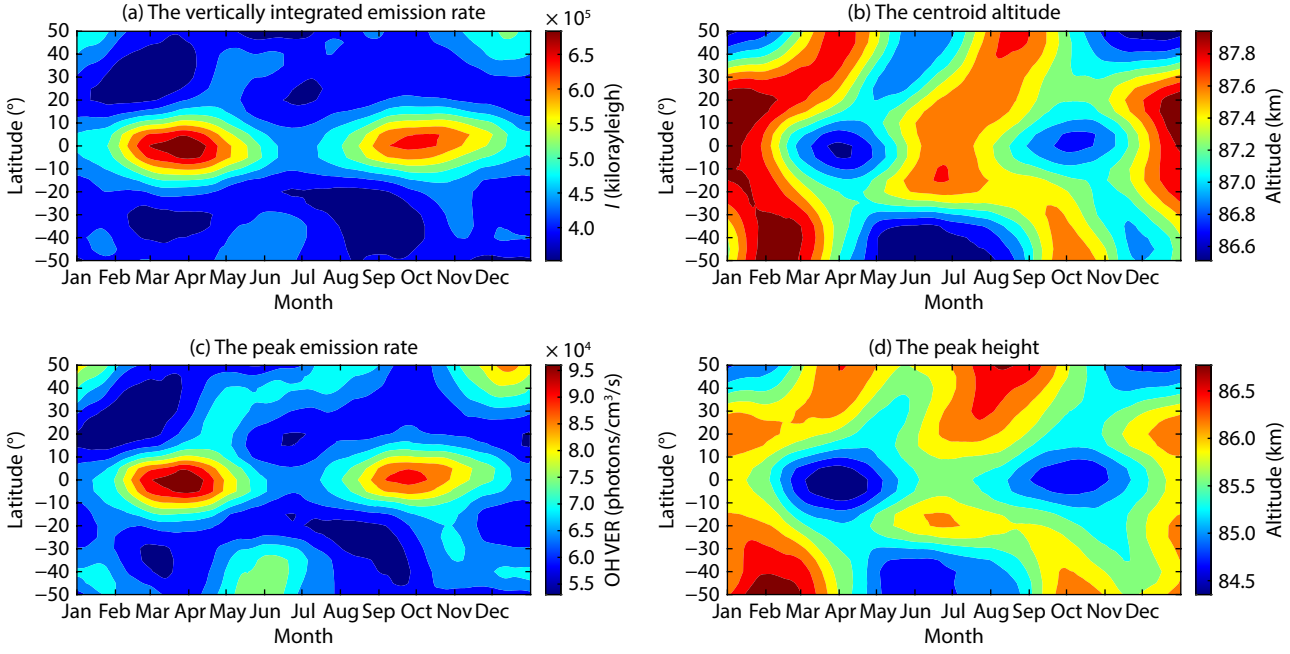

Figure 5. A superimposed year of peak OH airglow emission from 2003 to 2021. (a) Latitude–time distribution of the vertically integrated emission rate over multiple years. (b) Latitude–time distribution of the centroid altitude averaged over multiple years. (c) Latitude–time distribution of the peak emission rate over multiple years. (d) Latitude–time distribution of the peak height averaged over multiple years. VER, volume emission rate.

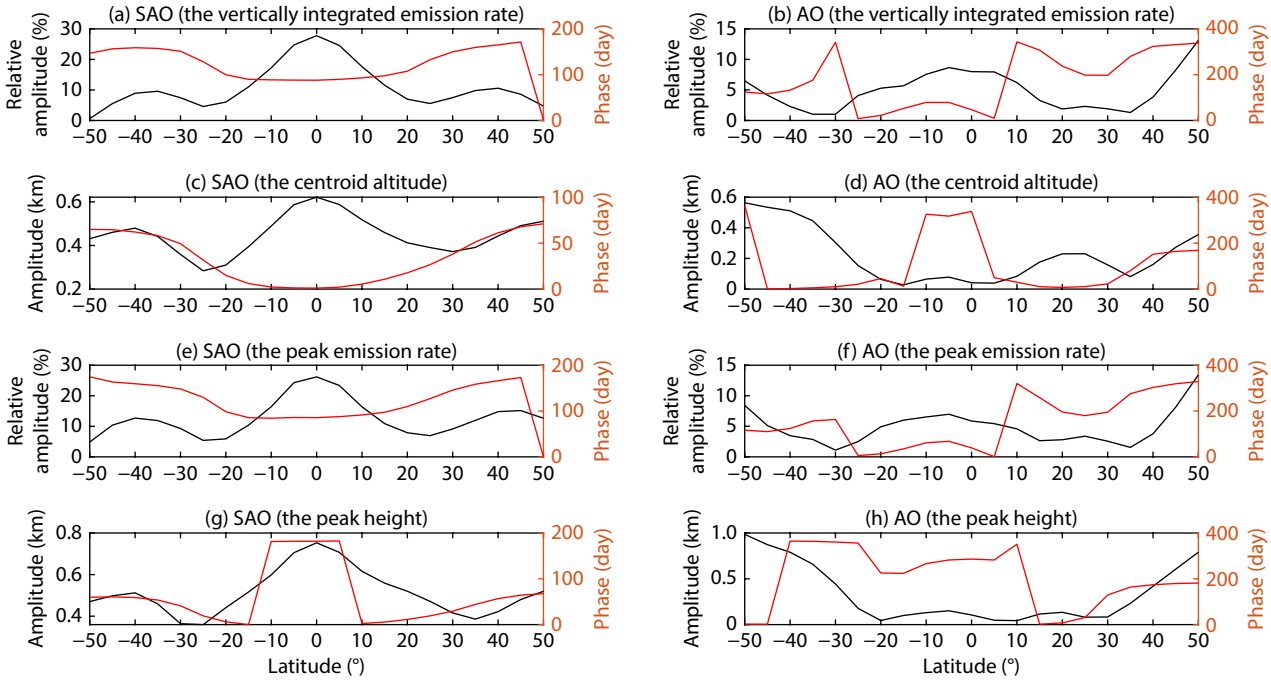

Figure 6. (a, b) Latitudinal distribution of the amplitudes and phases of the semiannual oscillation (SAO) and annual oscillation (AO) in the vertically integrated emission rate. (c, d) Latitudinal distribution of the amplitudes and phases of the SAO and AO in the centroid altitude. (e, f) Latitudinal distribution of the amplitudes and phases of the SAO and AO in the peak emission rate. (g, h) Latitudinal distribution of the amplitudes and phases of the SAO and AO in the peak height.

phenomenon, and the minimal value appears at the equinoxes. The OH emission peak height is inversely proportional to the peak emission rate. In the equatorial region, the minimum value of the peak height at the equinox corresponds to the maximum value of the peak emission rate. Previous studies have found the same phenomenon and concluded that tides affect the semiannual oscillation in OH emission (Yee et al., 1997; Melo et al., 1999).

To obtain the amplitudes and phases of semiannual and annual oscillation in the peak OH airglow emission, we used a harmonic fitting method, applying Equation (7):

$$f = f_0 + a \times \cos\left[\frac{2\pi}{183\,(\text{day})}\left(t - t_{\text{SAO}}\right)\right] + b \times \cos\left[\frac{2\pi}{365\,(\text{day})}\left(t - t_{\text{AO}}\right)\right], \quad (7)$$

where f can be I, Z, V_{max}, and h_{max}; f_0 denotes the multiyear average; t is the time index in days; and a and b are the amplitudes of the semiannual and annual oscillation. Times t_{SAO} and t_{AO} are the times at which the semiannual oscillation (SAO) and annual oscillation (AO) maxima occur. Figure 6 shows the amplitude and phase of the annual and semiannual oscillation of the four OH airglow parameters at different latitudes, respectively.

Figures 6a and 6b show the latitudinal variation of the vertically integrated emission rate relative amplitude in percentage terms: $(a/f_0) \times 100\%$, $(b/f_0) \times 100\%$. As shown in Figure 6a, semiannual oscillation amplitudes range from 0.8% to 23.5% with three peaks, with the largest amplitude of approximately 23.5% in the equatorial region. Looking at the phase of the semiannual oscillation, we can see that the maximum value of the amplitude in the equatorial region occurs on the 88th day of the year. The emission rate may be related to the diurnal tides and its seasonal variations may be caused by the seasonal variations of the diurnal tides. Later, we analyze the reason for the occurrence of semiannual oscillation in the OH emission. Notably, the emission rate in Figure 2 is anomalous in 2015, with the maximum value at the March equinox being smaller than the maximum value at the September equinox. We analyze the reason for this occurrence later.

As shown in Figure 6b, the relative amplitude of the annual oscillation is less than 13%. The amplitude of the annual oscillation is relatively large at higher latitudes, with the largest amplitude of 13% at 50°N, which is greater than 6% at 50°S. We noted the semiannual and annual variations in OH airglow intensity provided by Reid et al. (2014), who analyzed filter photometer measurements at Buckland Park (34.6°S, 138.6°E). They found a value of 7% for the semiannual oscillation, which peaked at day 160 and was in good agreement with our semiannual oscillation results. The annual oscillation was a poorer match; Reid et al. (2014) reported an amplitude of 14%, which is several times the amplitude of our results. The phase shows a maximum amplitude at day 159, in general agreement with our results.

The amplitude of the centroid altitude is the absolute amplitude rather than the relative amplitude, as shown in Figure 6c. The semiannual oscillation amplitude ranges from 0.2 to 0.55 km, with the largest amplitude of 0.55 km in the equatorial region and the maximum occurring on the first day of the year. The annual oscillation amplitude is very small at low latitudes and is dominant at higher latitudes. The amplitude of the annual oscillation near 50°S is the largest, at 0.52 km, with the maximum occurring on the 363rd day of the year, whereas the amplitude of the annual oscillation at 50°N is 0.33 km, occurring on the 167th day of the year. Figures 7e and 7f show the amplitude and phase of the semiannual and annual oscillation of the peak emission rate, treated in the same way as the vertically integrated emission rate. The amplitude and phase of the semiannual and annual oscillation of the peak emission rate are similar to those of the vertically integrated emission rate. The pattern of change is similar to that of I. Figures 6g and 6h show the peak height, which is treated in the same way as the centroid altitude. The pattern of change is somewhat similar to that of the centroid altitude. Unlike the centroid altitude, the amplitude of the annual oscillation in the peak heights is also largest near 50°S, approximately 0.9 km, but the maximum occurs at the beginning of the year.

Theoretical studies generally agree that atomic oxygen between 80 and 100 km is controlled largely by downward transport from the thermosphere, where its abundance is very large and its photochemical destruction rate is slow (Garcia and Solomon, 1985). Huang TY and Hickey (2007) noted that vertical transport becomes important when species have long lifetimes and small-scale heights. Because O has a relatively long chemical lifetime, O is mainly controlled by dynamics and is less affected by chemistry. For species like O_3 and OH*, which have smaller lifetimes, the combination of chemistry and dynamics leads to much greater variability in these species. We therefore chose to use atomic oxygen as a tracer to represent the dynamic processes, with heights corresponding to isodensity lines. Figure 7 depicts the zonal atomic oxygen concentration predicted by the SD-WACCM-X at the equator (0°) as a function of time and altitude, with the simulations corresponding to the four OH airglow parameters in Figure 2. Below 100 km, the rapid loss of atomic oxygen attributable to three-body recombination is replenished by downward transport, and the rate of loss increases as the altitude decreases. As shown in Figure 7, variations in the airglow emission rate and altitude are correlated with corresponding changes in the altitude of the atomic oxygen. As shown in Figure 7, changes in the airglow emission rate and height are correlated with changes in the atomic oxygen concentration (vertical transport). The lower the height to which atomic oxygen is transported, the greater the vertically integrated emission rate and the peak emission rate and the lower the centroid altitude and peak height.

As was noted above, a considerable amount of O is transported downward, resulting in an increase in O at lower altitudes. Because of an increased downward flux of O, an increased amount of O is available to recombine with the major gases. Consequently, a large amount of O_3 is created through the three-body recombination reaction (Equation (8)) caused by the increased O, and some of it is then destroyed in an exothermic reaction (Equation (1)) to produce OH*. Because OH* is mainly produced through Equation (1), it is not surprising to find a large net increase in the OH* number density because of the increased loss of O_3 via Equation (1). The increase in OH* is a direct result of the increase in the amount of O_3 reacting in Equation (1) and is an indirect result of the increase in O transported vertically. Huang TY and Hickey (2007) used a spectral full-wave dynamic model and a

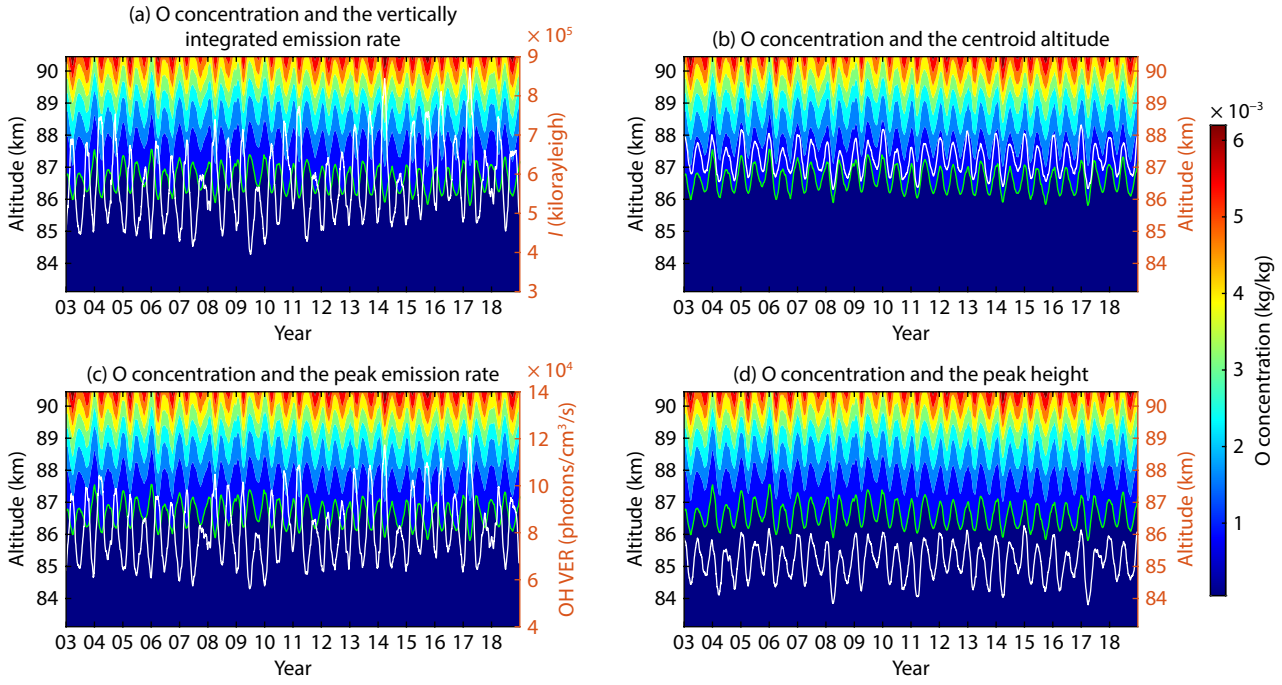

Figure 7. Contour plots of the zonal atomic oxygen concentrations in the equatorial (0°) zone predicted by the SD-WACCM-X are shown. The green line refers to the contour with an atomic oxygen concentration of 0.00048 kg/kg. The white line is the parameter describing the OH airglow. The white line is the vertically integrated emission rate (a), the centroid altitude (b), the peak emission rate (c), and the peak height (d).

2D OH chemistry model to investigate the latitudinal variations in the wave effects on the minor species in OH chemistry in the MLT region. They attributed the increase in the O number density at lower altitudes to wave transport and the increase in the number densities of O_3 and OH* to the combination of wave transport and chemical effects, with chemical effects dominating. They suggested that vertical wave transport of O coupled with chemistry could enhance the OH* volume emission rate because of a significant increase in the number density of the OH*. Therefore, the vertical motion of O coupled with chemistry does seem to play a significant role in the enhancement of the OH* volume emission rate. They noted that the vertical motion of the species could be due to the action of gravity waves or other types of waves, such as the tidal motion shown in Zhang SP and Shepherd (1999):

$$O + O_2 + M \xrightarrow{k_{O+O_2+M}} O_3 + M. \quad (8)$$

To investigate the correlation between OH emission, vertical transport of atomic oxygen, and the DW1, we extracted the heights corresponding to the equatorial contours with the atomic oxygen concentration of 0.00048 kg (indicated by the green line in Figure 7) and compared them with the peak emission rate and the amplitude of DW1, respectively. As shown in Figures 8a and 8b, the larger the DW1 amplitude, the lower the altitude to which the atomic oxygen is transported, and the larger the corresponding OH airglow emission. The DW1 amplitude data for a total of 19 years from 2003 to 2021 were averaged by superimposing them. A superimposed year was obtained that could be used to represent a multiyear average of DW1 amplitude. Figure 8c shows the DW1 amplitude after multiyear averaging. A clear semiannual oscillation can be seen in the equatorial region. The correlation coefficient between the calculated DW1 amplitude and the peak emission rate is shown in Figure 8d. We found that the correlation coefficient between the two is largest in the equatorial region where the DW1 amplitude is largest, at 0.87. The latitudinal dependence of DW1 can be used to explain the latitudinal dependence of the semiannual oscillation of the OH emission. In addition, Marsh et al. (2006) mentioned that annual oscillation in the higher latitude OH emission is consistent with transport by the downward component of the mean meridional circulation, which brings air rich in atomic oxygen from the lower thermosphere into the mesopause region.

3.4 Modulation by Quasibiennial Oscillation

The quasibiennial oscillation is a tropical, lower stratospheric, downward-propagating zonal wind variation, with an average period of ~28 months. The importance of the quasibiennial oscillation is that it dominates the variability of the tropical lower stratospheric meteorology (Wallace, 1973). The quasibiennial oscillation is also important for seasonal forecasting, and it controls stratospheric ozone and water variability that can modulate surface ultraviolet and infrared radiation. In this work, we used the zonal wind at 11 hPa above Singapore to represent the stratospheric quasibiennial oscillation. At low latitudes, where semiannual oscillation dominates the OH airglow emission, Burrage et al. (1996) analyzed horizontal wind field measurements obtained from 1992 to 1995 by the High-Resolution Doppler Imager experiment on UARS and found an oscillation with a period of approximately 2 years. The maximum amplitude occurred near an altitude of 85 km, which corresponds to the peak height in our results. The mesopause quasibiennial oscillation shows the same altitudinal and latitudinal structure as the mesopause semiannual oscillation and exhibits a phase relationship with the stratospheric quasibiennial oscillation, suggesting

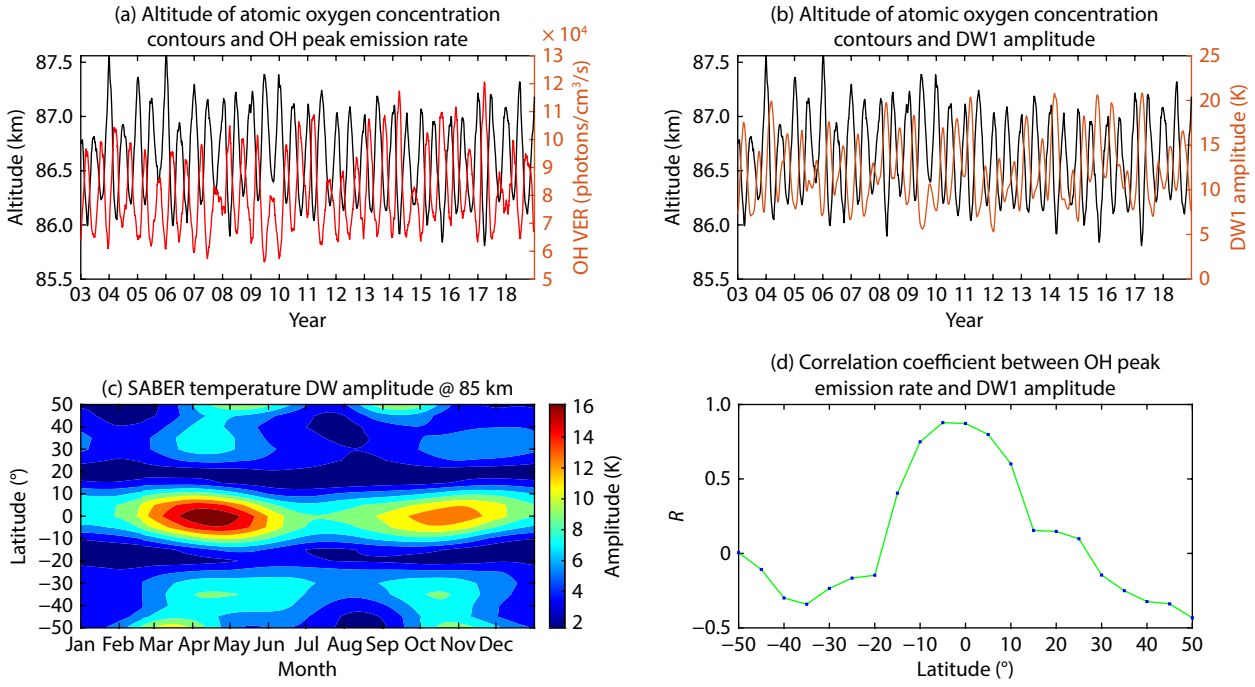

Figure 8. (a) We used the altitude corresponding to the atomic oxygen concentration of 0.00048 kg/kg (black line) to denote the vertical transport of atomic oxygen, and the red line to denote the OH peak emission rate. (b) Vertical transport of atomic oxygen and the amplitude of the DW1. (c) A superimposed year of DW1 amplitude from Figure 4d. (d) Latitudinal dependence of the correlation coefficients of the OH peak emission rate and DW1 amplitude.

that the mesopause semiannual oscillation is modulated by the stratospheric quasibiennial oscillation. In addition, a mesopause quasibiennial oscillation was detected by the Christmas Island medium-frequency radar (2°N, 130°W), with the same phase and the same peak height as the mesopause quasibiennial oscillation shown by the HRDI. Although the amplitude is only half that shown by the HRDI, this observation also confirms the existence of the mesopause quasibiennial oscillation.

To facilitate the analysis of the relationship between OH airglow emission and the stratospheric quasibiennial oscillation, we chose a 365-day sliding temporal window with a step of 1 day to smooth OH emission rates and heights, to avoid the effect of seasonal variations on the analysis of the results. The smoothed results shown in Figure 9 indicate the vertically integrated emission rate, centroid altitude, peak emission rate, and peak height, respectively.

Figure 9a shows the latitude–time distribution of the vertically integrated emission rate, with the white line being the daily average of the equatorial stratospheric zonal winds. After smoothing, we found that in the equatorial region, the quasibiennial oscillation signal in the OH airglow emission may be related to the quasibiennial oscillation signal in the stratospheric zonal winds. The peak emission rate of the quasibiennial oscillation signal is much weaker in the higher latitude region than in the equatorial region, which is also consistent with previous findings (Marsh et al., 2006; Shepherd et al., 2006). The variation in emission rate in the equatorial region is correlated with the phase change of the 11 hPa tropical zonal winds in Singapore. The emission rate is relatively large during westerly phases (e.g., in 2006) and relatively small during easterly phases (e.g., 2007). It is worth noting that the anomalies in OH airglow emission in 2015 mentioned above are associated with stratospheric quasibiennial oscillation anomalies. The quasibiennial oscillation anomalies in the OH airglow emission rate from 2015 to 2016 correspond to the anomalous changes in quasibiennial oscillation observed in radio soundings by Newman et al. (2016), which also confirms that OH airglow emission at 85 km is indeed affected by quasibiennial oscillation in the tropical stratosphere influence.

Figure 9b shows the latitude–time distribution of the centroid altitude. In the equatorial region, the emission height is modulated by the quasibiennial oscillation, as is the emission rate. Of course, because the emission height is inversely proportional to the emission rate, the emission altitude is low during the westerly phase. The quasibiennial oscillation signal for the centroid altitude is also weak at higher latitudes. The characteristics of the quasibiennial oscillation signal in the peak emission rate of Figure 9c and the peak height of Figure 9d are similar to those in the vertically integrated emission rate and the centroid altitude, respectively.

The quasibiennial oscillation signal in the equatorial region has been the subject of many related studies. Xu JY et al. (2009) analyzed the quasibiennial oscillation of the migrating diurnal tide based on temperature and wind data from TIMED observations. After comparison, we found that the distribution of OH airglow emission at low latitudes is similar to that of the migrating diurnal tide in temperature. The quasibiennial oscillation phenomenon is more pronounced in equatorial regions compared with higher latitudes because of the dominant tidal influence on OH airglow emission at lower latitudes. Pramitha et al. (2021)

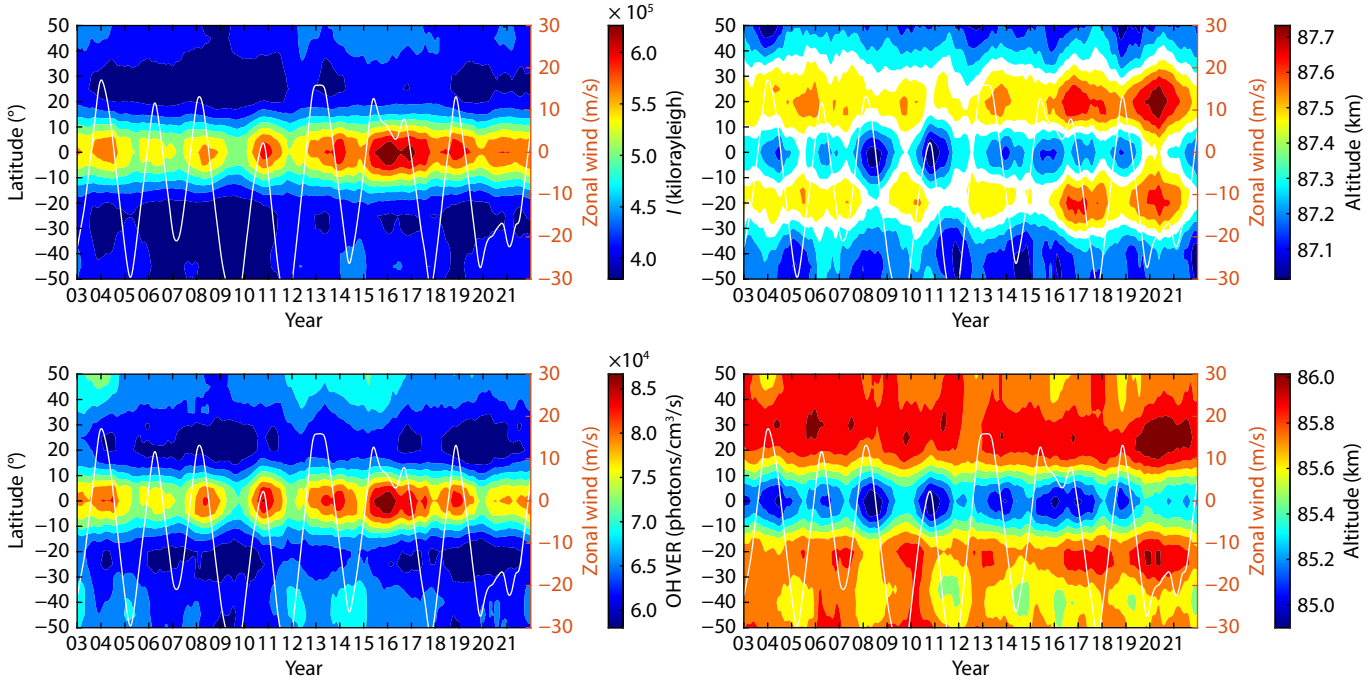

Figure 9. (a) Latitude–time distribution of the vertically integrated emission rate I. (b) Latitude–time distribution of the centroid altitude Z. (c) Latitude–time distribution of the peak emission rate V_{max}. (d) Latitude–time distribution of the peak height h_{max}. The white line refers to the daily average of the equatorial stratospheric zonal winds, smoothed like the four parameters of the OH airglow. A positive wind speed indicates an eastward wind. VER, volume emission rate.

found a good correspondence between the MLT diurnal tide and the stratospheric quasibiennial oscillation based on meteor radar observations and WACCM simulations. Regarding how the stratospheric quasibiennial oscillation modulates the emission of OH airglow, Shepherd et al. (2006) found a decrease in the center of the airglow emission maximum during quasibiennial oscillation modulation, indicating the downward transport of atomic oxygen. This result is also verified by the significant decrease in peak height (Figure 9b) when the zonal wind is eastward compared with when the zonal wind is westward. The authors suggested that the tidal influence on the mesospheric airglow emission is due to a corresponding tidal change in the atomic oxygen mixing ratio caused by vertical motion. To analyze whether the quasibiennial oscillation signal in the OH emission is tidally correlated, we first smoothed the tidal amplitude from Figure 4d; the result is shown in Figure 10a. The quasibiennial oscillation signal is also shown in the diurnal tidal amplitude. Because quasibiennial oscillation modulation of the OH emission is also tidally correlated, we wanted to know whether it would be observed in the vertical transport of atomic oxygen as in the semi-annual oscillation.

For OH airglow data, we chose the data in Figure 2 for the time

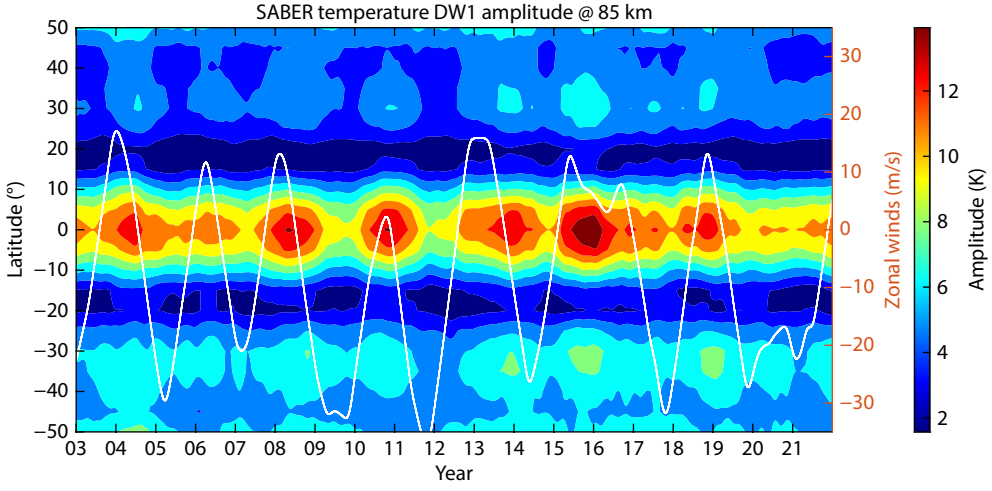

Figure 10. (a) Latitude–time distribution of the 85-km diurnal tide amplitude. The white line refers to the daily average of the equatorial stratospheric zonal winds, smoothed like the four parameters of the OH airglow. A positive wind speed indicates an eastward wind.

range of 2004–2020 and derived the monthly average. Because of the phase of the quasibiennial oscillation shift in altitude, we used a longer time series of Singapore wind that began 24 months before and ended 24 months after (to cover one quasibiennial oscillation period) the SABER OH airglow data and shifted it month by month to find the best agreement, quantified by the correlation coefficient. As shown in Figure 11, in the equatorial region, there is a 3-month delay in the OH emission rate compared with the wind field at 11 hPa in Singapore, which is in general agreement with the findings of Teiser and von Savigny (2017) on the delay in the OH(3-1) band compared with the wind field at 15 hPa in Singapore.

The left side of Figure 12 shows the equatorial OH time series with the corresponding Singapore wind time series. Shown in Figure 12a are the vertically integrated emission rate and Singapore wind data. The OH time series began in January 2004, and the Singapore wind time series began in October 2003, with a 3-month phase difference between them. The quasibiennial oscillation signal of OH emission near the equator has a delay of approximately 3 months compared with the stratospheric quasibiennial oscillation. Figures 12b, 12c, and 12d correspond to Z, V_{max}, and h_{max}, respectively. The correlation coefficients of the OH time series with the Singapore wind time series are shown on the right. The black line corresponds to the Singapore wind time series as a shifted quasibiennial oscillation, whereas the red line indicates the real Singapore wind time series. The correlation coefficients between emission and quasibiennial oscillation are large in the region around the equator and 30°N/S, and the semiannual oscillation amplitude of the emission rate is extreme in these latitudes. From the previous analyses, we speculate that the semiannual oscillations of the emission rate are tidally related. The quasibiennial oscillation signal in the emission rate shows a latitudinal structure similar to the semiannual oscillation, which we believe may be caused by the fact that the quasibiennial oscillation in the OH emission is also tidally related.

3.5 Modulation by Solar Activity

In addition to seasonal variations, at some latitudes, such as near 50° latitude, the OH airglow emission rates are greater in 2002–2003 and 2014–2015 than near 2008–2009 and 2019–2020. Airglow is very sensitive to atmospheric conditions, and solar variations also affect atmospheric conditions such as temperature and gas concentration, with any change in temperature or gas concentration leading to changes in airglow intensity. Because solar radiation directly drives the production of atomic oxygen, OH airglow emission varies with (i.e., is modulated by) solar activity. To explore the correlation between OH airglow emission and solar activity, and the response of the emission rates to changes in solar activity, we used the SABER data and the $F_{10.7}$ solar index.

Figure 13a represents the latitudinal time distribution of I, and Figure 13b represents the latitudinal time distribution of Z. As shown in the figure, the response of OH airglow emissivity to solar activity changes at different latitudes is not synchronized, and a more pronounced gap can be seen between the response time at the equator and the response time at mid-latitudes. Figure 13c shows the global year average of I and $F_{10.7}$ in 2004–2020, and Figure 13d shows the global year average of Z and $F_{10.7}$ in 2004–2020. The correlation coefficient between the vertically integrated emission rate and solar activity is 0.45, and the correlation coefficient between the centroid emission altitude and solar activity is –0.58. The correlation coefficient between the peak emission rate and solar activity is 0.88, and the correlation coefficient between the peak height and solar activity is –0.66, as shown in Figures 14c and 14d.

A global annual mean series scatterplot between I and $F_{10.7}$ is

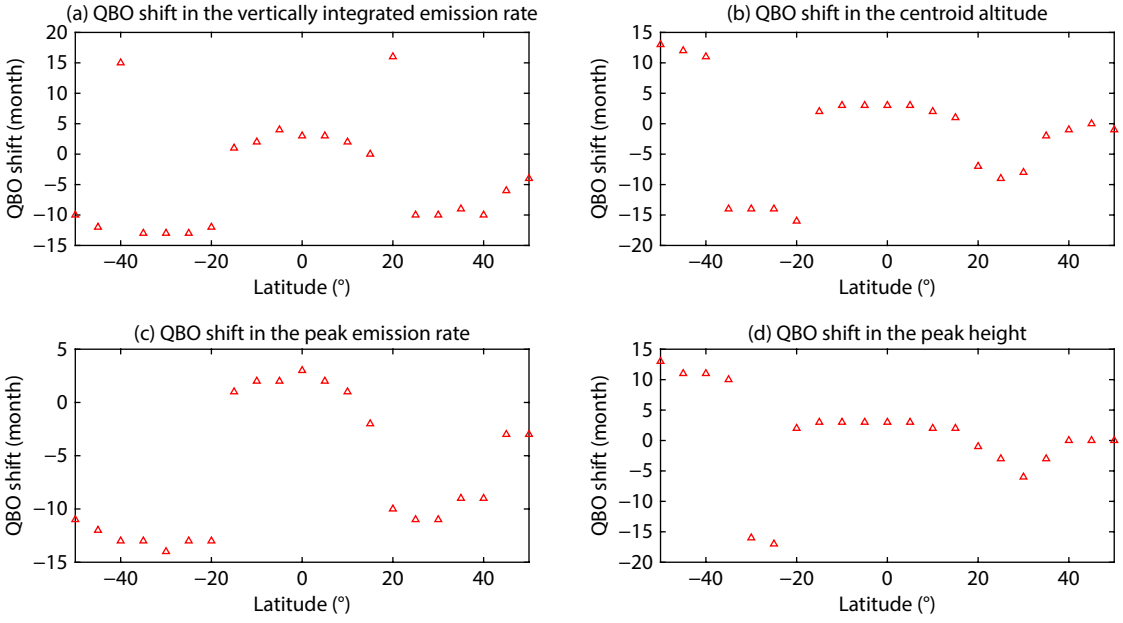

Figure 11. Latitude variations of the quasibiennial oscillation (QBO) shift for the emission rate (left) and the emission altitude (right). (a) The shift of the vertically integrated emission rate; (b) the shift of the centroid altitude; (c) the shift of the peak emission rate; and (d) the shift of the peak height. A shift by 3 months meant that the Singapore wind time series began in October 2003, whereas the OH time series began in January 2004.

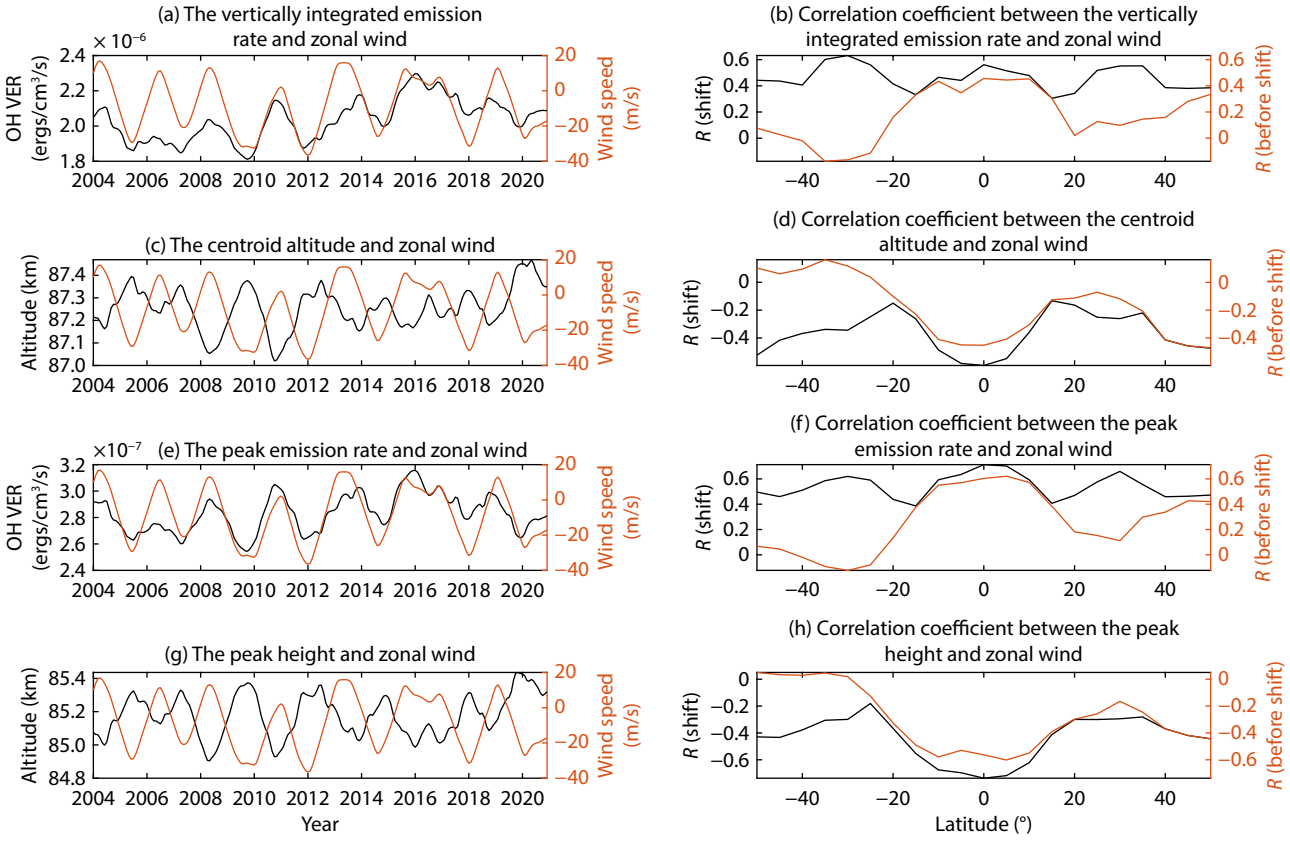

Figure 12. (Left) The equatorial OH time series and the corresponding Singapore wind time series. Vertically integrated emission rates and Singapore wind data are shown in (a). Panels (b), (c), and (d) correspond to the centroid altitude, the peak emission rate, and the peak height, respectively. (Right) Correlation coefficients between the OH time series and the Singapore wind time series. The black line corresponds to the Singapore wind time series as a shifted quasibiennial oscillation, whereas the red line represents the real Singapore wind time series. VER, volume emission rate.

shown in Figure 13e, and Z, V_{max}, and h_{max} are shown in Figures 13f, 14e, and 14f, respectively. From Figures 14c and 14e, we found that the global year average of V_{max} has an apparent linear relationship with the corresponding annual average of $F_{10.7}$. Assuming a linear relationship, we used linear regression to calculate the solar response of OH airglow emission:

$$f = A + B \times F_{10.7}, \tag{9}$$

where B is the slope of the linear regression equation and A is its ordinate at the origin; that is, A is a constant and B is the coefficient of linear fit derived from the least-squares regression analysis, representing the solar response to the OH airglow emission. Using least-squares regression calculations, we obtained the global response of the OH airglow emission to solar activity and its standard deviation. The solar response value for I is $(2.5 \pm 1.26) \times 10^4$ kilorayleigh/100 sfu, the solar response value for Z is (-0.07 ± 0.02) km/100 sfu, the solar response value for V_{max} is $(5.21 \pm 0.73) \times 10^3$ photons/cm^3/s/100 sfu and the solar response value for h_{max} is (-0.07 ± 0.02) km/100 sfu.

Through correlation analysis of the yearly average series for each latitude bin, we obtained the correlation coefficients between OH emission and $F_{10.7}$ for 21 latitude zones; the results are shown in Figure 15. Figures 15a–15d represent the correlation coefficients of I, Z, V_{max}, and h_{max}, respectively. The absolute minimum of the correlation coefficients for these covariates, except for the peak height, is near the equator. In particular, the correlation coefficients for the southern hemisphere are significantly higher than those for the corresponding latitudes in the northern hemisphere. We do not know the reason for the lower correlation coefficients at high northern latitudes.

Teng CKM et al. (2021) used SD-WACCM-X and the residual circulation principle to study the global atmospheric circulation from the lower atmosphere to the upper atmosphere (~500 km) from 2002 to 2019. They found that the atmospheric circulation at mid- and high-latitude regions is more influenced by solar activity than that at low latitudes and equatorial regions. Laskar et al. (2014) found that the effect of planetary waves and the coupling of planetary waves and tides on the upper atmosphere varies with solar activity. These may contribute to the latitudinal dependence of the airglow response to solar activity.

We obtained the latitudinal distribution of the response of OH to solar activity and its standard deviation by using a least-squares regression. Figure 16 shows the magnitude of the response of OH to solar activity and its standard deviation for each latitude bin. For I and V, the range of solar response increases essentially from the equator to 50°N/S. In each hemisphere, the standard deviation of the solar response decreases from the equator to 50°N/S. The correlation coefficients are correlated with the corresponding

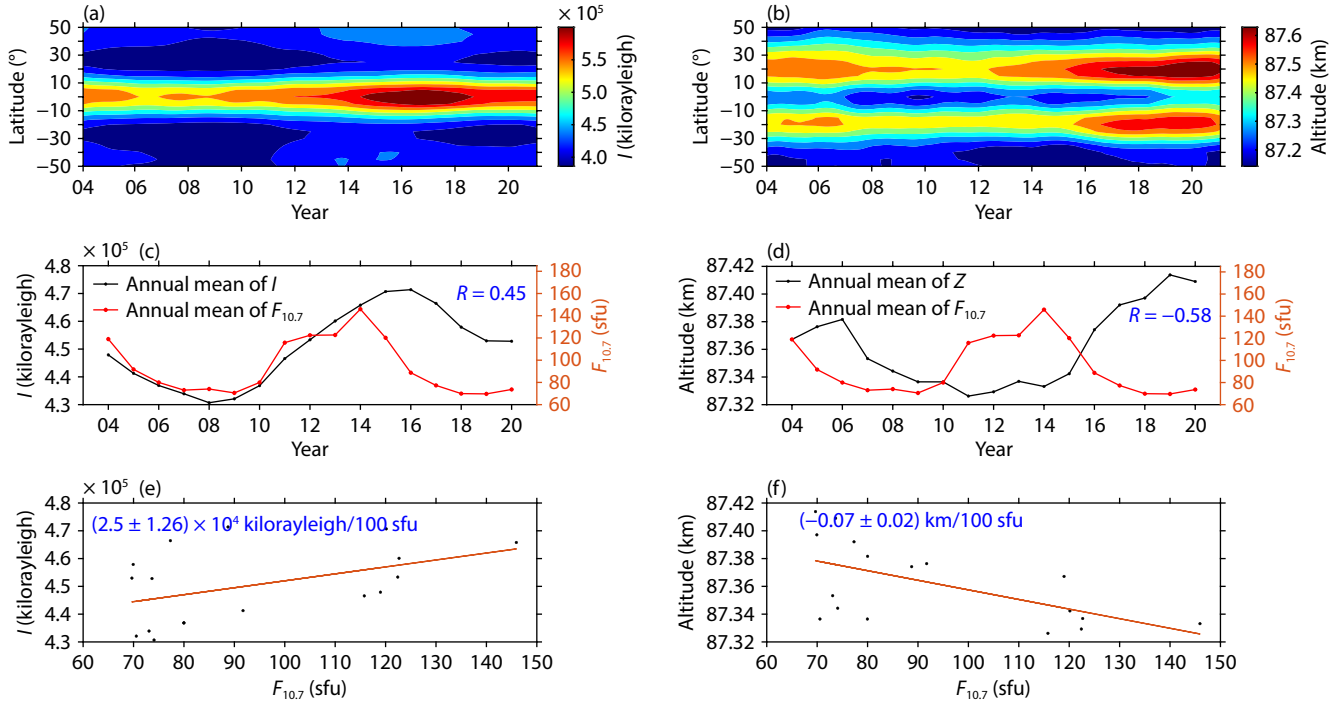

Figure 13. The interannual variations of OH airglow emission. (a) Latitude–time distribution of I (the vertically integrated emission rate). Emission rates are smoothed over a window length of 3 years. (b) Latitude–time distribution of Z (the centroid altitude). (c) The global year average of I and $F_{10.7}$ in 2004–2020. (d) The global year average of Z and $F_{10.7}$ in 2004–2020. (e) The scatterplot of $F_{10.7}$ and I, and the solar response value of I. (f) The scatterplot of $F_{10.7}$ and Z, and the solar response value of Z.

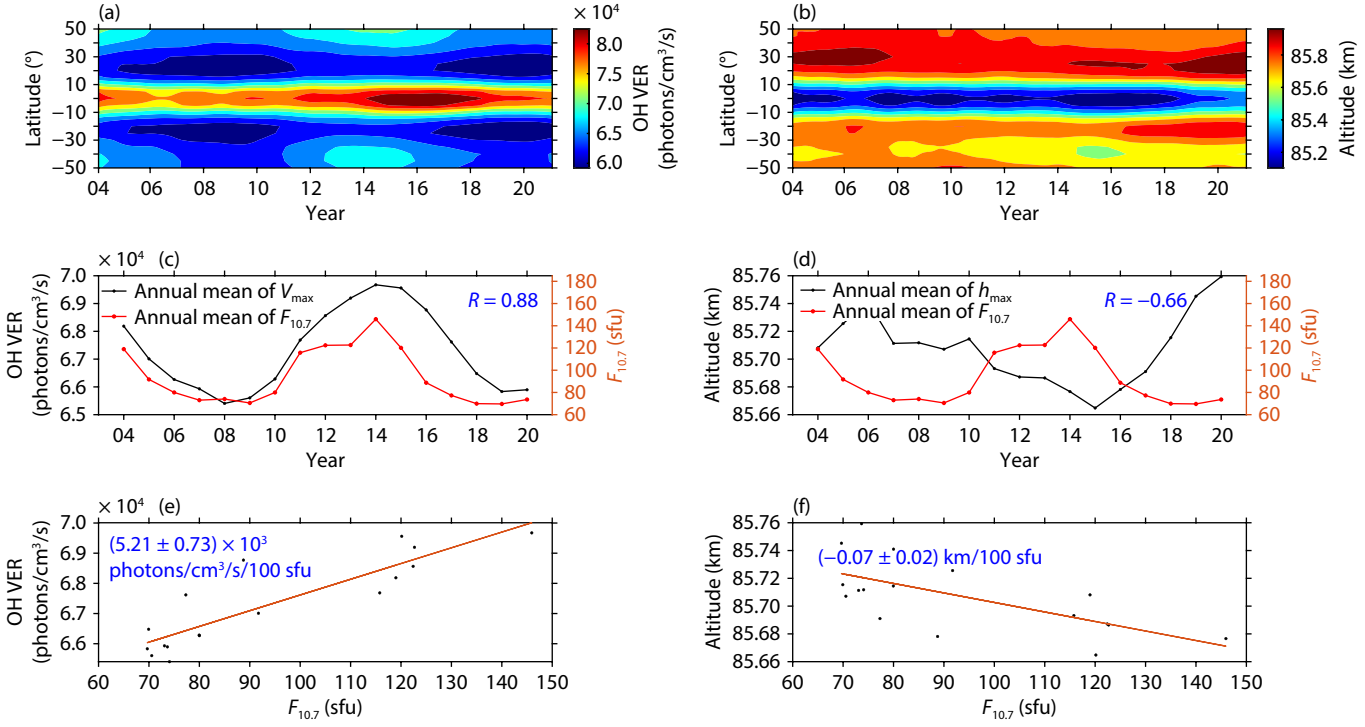

Figure 14. The interannual variations of OH airglow emission. (a) Latitude–time distribution of V_{max} (the peak emission rate). Emission rates are smoothed over a window length of 3 years. (b) Latitude–time distribution of h_{max} (the peak height). (c) The global year average of V_{max} and $F_{10.7}$ during 2004–2020. (d) The global year average of h_{max} and $F_{10.7}$ in 2004–2020. (e) The scatterplot of $F_{10.7}$ and V_{max}, and the solar response value of V_{max}. (f) The scatterplot of $F_{10.7}$ and h_{max}, and the solar response value of h_{max}. VER, volume emission rate.

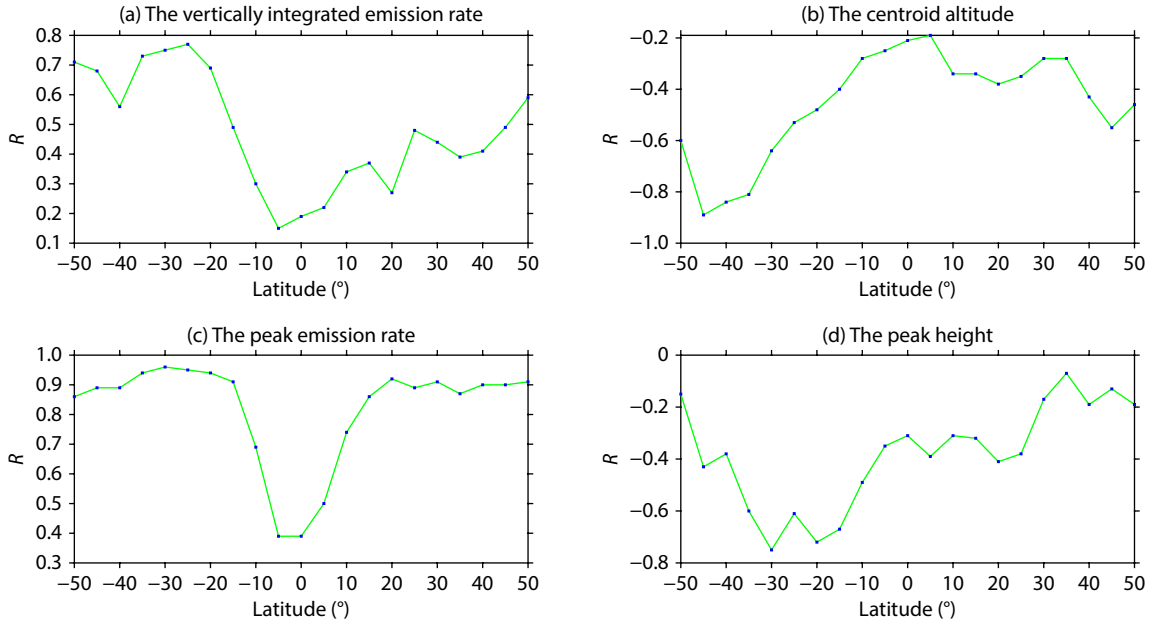

Figure 15. The correlation coefficients between OH emission and $F_{10.7}$ for 21 latitude zones.

range of fluctuations in the solar response: the higher the correlation coefficient, the greater the amplitude. However, the latitudinal profile of the solar response for emission heights, especially peak heights, does not show a significant correlation with the emission rate. Tang CL et al. (2018) investigated the correlation between ozone concentration and solar activity by using broadband emission radiometric atmospheric sounding (SABER) measurements and the 10.7-cm solar radio flux ($F_{10.7}$) dataset. He noted that O_3 is determined by many factors under the radiative, chemical, and dynamic processes. With an increase in ultraviolet irradiance, the solar activity index $F_{10.7}$ increases, the production of ion pairs by photoionization (N_2 and O_2) increases, and the production of atoms by O_2 photodissociation increases; thus, the abundance of O atoms varies with solar activity. The photochemical formation of ozone depends on solar activity.

Ozone concentrations are determined by a balance between production via Equation (8) and losses through photolysis and Equation (1). Assuming photochemical equilibrium, and equating production to loss,

$$[O_3] = \frac{k[O][O_2][M]}{J_{O_3} + k'[H]},$$

where [ ] denotes the number density, k and k' are kinetic rate constants for Equation (8) and (1), J_{O_3} is the ozone photolysis rate (approximately 100 s^{-1}), and M is a third body (i.e., O, O_2, N_2). Marsh et al. (2007) presented new simulations of the "whole

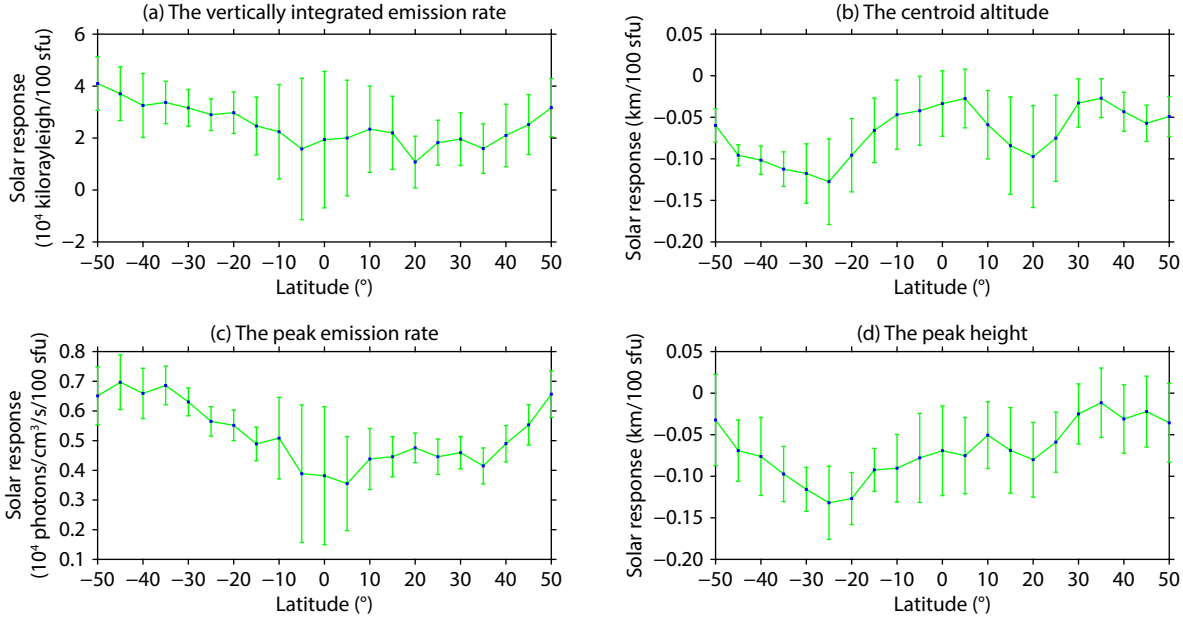

Figure 16. The solar response ranges of OH emission for 21 latitude zones. The vertical bars show the standard deviation of the solar response.

atmosphere" response to variability in solar and geomagnetic forcing by using a 3D general circulation model with fully interactive chemistry. Changes in the solar activity affect the daytime production of atomic oxygen and hydrogen by photolysis. Simulations show that atomic oxygen also increases during solar maximum by 30%–50%, so production rates should increase accordingly. During the daytime, the loss mechanism is primarily via photolysis in the Hartley and Huggins bands (200–350 nm), which change just a few percent over the solar cycle. Therefore, solar-induced changes in the daytime equilibrium value of ozone are very similar to the changes in atomic oxygen. As already discussed by Marsh et al. (2006), the drop in intensity is probably caused by the consumption of atomic oxygen, which is mostly produced at daytime because of the photolysis of molecular oxygen. This also explains why the OH airglow intensity is greater in years of high solar activity than in years of low solar activity.

Marsh et al. (2006) compared SABER observations with a 3D chemical transport model and found that most of the change in emissions was due to changes in ozone. Vertical transport of atomic oxygen is not the most important in the modulation of OH emission by solar activity. This finding may help explain why the solar response in emission height does not show a strong correlation with the solar response in emission rate. The intensity of solar radiation received at low latitudes is greater than at high latitudes, so changes in solar activity have a relatively small effect on the atmosphere at low latitudes. The composition and structure of the atmosphere at low latitudes are different from those at high latitudes, and the Earth's magnetic field is more complex at high latitudes, which may lead to greater sensitivity to changes in solar activity at high latitudes and a relatively smaller response at low latitudes. The latitudinal dependence of the solar response to OH airglow radiation is a result of a combination of factors. However, the exact physical mechanisms responsible for the latitudinal structures of the responses in this study cannot yet be verified, and a global chemistry–dynamics model including large-scale atmospheric circulation and waves is needed to answer this question.

Figure 17 illustrates the mechanism by which semiannual oscillation, quasibiennial oscillation, and solar activity regulate OH airglow emission. Marsh et al. (2006) compared model and observational data and found that most of the variability in OH airglow emission is caused by changes in the production rate of ozone. At the height of the peak emission, the variation is mainly caused by changes in atomic oxygen attributable to vertical transport. Atomic oxygen has a relatively long chemical lifetime, and the vertical transport of O coupled with the chemistry affects OH emission. Atomic oxygen produces large amounts of O_3 through reactions, and some of the O_3 is then destroyed in reactions with H to produce OH*. The vertical transport of atomic oxygen reacts to the seasonality and quasibiennial oscillation of the tidal amplitude, and the change in atomic oxygen will cause the change in O_3, which in turn affects the OH emission. The OH emission is positively correlated with solar activity, and emission height is inversely correlated with solar activity. The solar activity response of OH airglow emission, where the response of the emissivity is larger than the response of the emission height, suggests that the solar activity modulates the OH emission mainly by influencing chemical processes rather than dynamic processes.

4. Conclusions

In this article, the vertically integrated emission rate, centroid altitude, peak emission rate, and peak height of the OH airglow were calculated based on OH airglow emission data observed by the TIMED/SABER satellites from 2002 to 2022. These were used to study the variations in the intensity and location of OH emission and to analyze seasonal and interannual variations in emission rate and height. Using Lomb–Scargle periodograms analyses, we found semiannual and annual oscillations at both emission rate and height. After superimposing and averaging the emission rate and height, we used harmonic fitting methods to obtain the amplitude and phase of the semiannual and annual oscillations. The semiannual oscillation amplitude is largest in the equatorial region, with the maximum amplitude of the emission rate occurring on the 88th day of the year (near the spring equinox) and the maximum amplitude of the emission height occurring at the beginning of the year. At higher latitudes, annual oscillation dominates, with the maximum amplitude of the emission rate at 50°N and the maximum amplitude of the emission height at 50°S. The semiannual oscillation amplitude of the diurnal tides in the equatorial region is the largest, and the maximum occurs near the spring equinox. To analyze the cause of the semiannual oscillation, we calculated the diurnal tidal amplitude near the peak height of 85 km by using temperature data from SABER observations. We found that the tidal amplitude variation is in good agreement with the variation in OH airglow emission. The variation

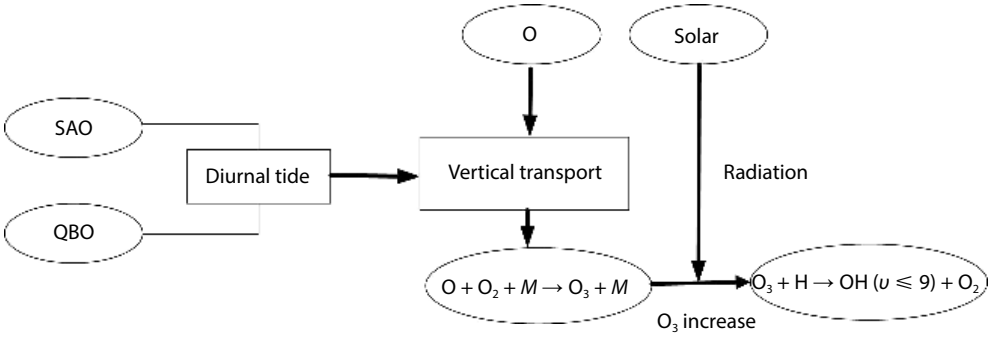

Figure 17. Schematic representation of the mechanism by which the OH airglow emission is modulated by semiannual oscillation (SAO), quasibiennial oscillation (QBO), and solar activity.

in ozone has an important effect on OH emission, and ozone production is closely related to atomic oxygen. We suggest that the tides may be influencing the vertical transport of atomic oxygen by affecting, in turn, the O_3 associated with the production of OH*. To investigate the correlation between the vertical transport of atomic oxygen and the tidal amplitude, we calculated the heights corresponding to the contours to represent the vertical transport of atomic oxygen by using the atomic oxygen concentration of the SD-WACCM-X. The calculation of the correlation between the vertical transport of atomic oxygen and the tidal amplitude revealed a strong correlation between the two. The latitudes where the correlation between the two is strong, such as the equator, are precisely the latitudes where the semiannual oscillation amplitude in OH emission is larger, which confirms that the tides have an important influence on OH emission.

In addition to the seasonal variations, we found a quasibiennial oscillation signal in the OH emission. Quasibiennial oscillation is also present in the diurnal tidal amplitude in the equatorial region, and both are significantly correlated with the Singapore zonal wind (denoted as stratospheric quasibiennial oscillation). By calculating the shift and correlation coefficients between the OH emission and the Singapore zonal winds at different latitudes, we found that the correlation coefficient is largest in the equatorial region, with a shift of approximately 2 months. In addition, the correlation coefficients of the emission rates have peaks near 30°N/S. The correlation coefficients of the emission rates are also higher in the equatorial region. This result is similar to the latitudinal variation of the semiannual oscillation amplitude of the OH emission, which also suggests that the quasibiennial oscillation signal of the OH emission is consistent with the cause of semiannual oscillation production, which is mainly due to the vertical transport of atomic oxygen.

Finally, we analyzed the relationship between OH emission and solar activity. There is no doubt that OH emission must be modulated by solar activity, and after calculating the correlation coefficients between the mean annual change in OH emission and the mean annual change in $F_{10.7}$, we then analyzed the response of OH emission to solar activity at different latitudes. We found that the effect of higher latitude solar activity on OH emission is greater than the effect of low-latitude and equatorial solar activity on OH emission. The solar response of OH emission in the southern hemisphere is larger than that of OH emission at the same latitude in the northern hemisphere. The photochemical formation of O_3 is dependent on solar activity and has an important effect on OH emission. The strong solar response for emission and the weak solar response for emission height indicate that solar activity modulates OH emission mainly through chemical rather than dynamic processes.

Data availability

The SABER data can be accessed via https://saber.gats-inc.com. The MERRA-2 data (MERRA2_300.tavg_) can be accessed via http://disc.gsfc.nasa.gov. The $F_{10.7}$ solar index can be accessed via https://omniweb.gsfc.nasa.gov/form/dx1.html. The WACCM-X is open-source software, and the source code is publicly available at https://escomp.github.io/CESM/releasecesm2/downloading_cesm.html#downloading-the-code-and-scripts (accessed on October 18, 2019). The atmospheric forcing data, which were regridded from the MERRA-2 data set and used to run SD-WACCM-X, can be downloaded at https://rda.ucar.edu/datasets/ds313.3/?hash=access (accessed on October 18, 2019). The numerical calculations in this article were performed on the supercomputing system at the Supercomputing Center of Wuhan University.

Acknowledgments

This research was supported by the National Natural Science Foundation of China (Grant Numbers 42374195 and 42188101) and a fellowship from the China National Postdoctoral Program for Innovative Talents (Grant Number BX20230273).

References

Abreu, V. J., and Yee, J. H. (1989). Diurnal and seasonal variation of the nighttime OH (8-3) emission at low latitudes. *J. Geophys. Res.: Space Phys.*, *94*(A9), 11949–11957. https://doi.org/10.1029/JA094iA09p11949

Baker, D. J., Thurgood, B. K., Harrison, W. K., Mlynczak, M. G., and Russell, J. M. (2007). Equatorial enhancement of the nighttime OH mesospheric infrared airglow. *Phys. Scr.*, *75*(5), 615–619. https://doi.org/10.1088/0031-8949/75/5/004

Batista, P. P., Takahashi, H., and Clemesha, B. R. (1994). Solar cycle and the QBO effect on the mesospheric temperature and nightglow emissions at a low latitude station. *Adv. Space Res.*, *14*(9), 221–224. https://doi.org/10.1016/0273-1177(94)90139-2

Buriti, R. A., Takahashi, H., Gobbi, D., de Medeiros, A. F., Nepomuceno, A. A., and Lima, L. M. (2004). Semiannual oscillation of the mesospheric airglow at 7.4°S during the PSMOS observation period of 1998-2001. *J. Atmos. Sol. Terr. Phys.*, *66*(6-9), 567–572. https://doi.org/10.1016/j.jastp.2004.01.009

Burrage, M. D., Vincent, R. A., Mayr, H. G., Skinner, W. R., Arnold, N. F., and Hays, P. B. (1996). Long-term variability in the equatorial middle atmosphere zonal wind. *J. Geophys. Res.: Atmos.*, *101*(D8), 12847–12854. https://doi.org/10.1029/96jd00575

Gao, H., Xu, J. Y., and Wu, Q. A. (2010). Seasonal and QBO variations in the OH nightglow emission observed by TIMED/SABER. *J. Geophys. Res.: Space Phys.*, *115*(A6), A06313. https://doi.org/10.1029/2009ja014641

Gao, H., Xu, J. Y., and Chen, G. M. (2016). The responses of the nightglow emissions observed by the TIMED/SABER satellite to solar radiation. *J. Geophys. Res.: Space Phys.*, *121*(2), 1627–1642. https://doi.org/10.1002/2015JA021624

Garcia, R. R., and Solomon, S. (1985). The effect of breaking gravity waves on the dynamics and chemical composition of the mesosphere and lower thermosphere. *J. Geophys. Res.: Atmos.*, *90*(D2), 3850–3868. https://doi.org/10.1029/JD090iD02p03850

Huang, T. Y., and Hickey, M. (2007). On the latitudinal variations of the non-periodic response of minor species induced by a dissipative gravity-wave packet in the MLT region. *J. Atmos. Sol. Terr. Phys.*, *69*(6), 741–757. https://doi.org/10.1016/j.jastp.2007.01.011

Huang, T. Y. (2016). Simulations of airglow variations induced by the CO_2 increase and solar cycle variation from 1980 to 1991. *J. Atmos. Sol. Terr. Phys.*, *147*, 138–147. https://doi.org/10.1016/j.jastp.2016.07.014

Laskar, F. I., Pallamraju, D., and Veenadhari, B. (2014). Vertical coupling of atmospheres: dependence on strength of sudden stratospheric warming and solar activity. *Earth Planets Space*, *66*, 94. https://doi.org/10.1186/1880-5981-66-94

Liu, G., and Shepherd, G. G. (2006). An empirical model for the altitude of the OH nightglow emission. *Geophys. Res. Lett.*, *33*(9), L09805. https://doi.org/10.1029/2005gl025297

López-González, M. J., Rodríguez, E., Wiens, R. H., Shepherd, G. G., Sargoytchev, S., Brown, S., Shepherd, M. G., Aushev, V. M., López-Moreno, J. J., ... Cho, Y. M. (2004). Seasonal variations of O_2 atmospheric and OH(6-2) airglow and temperature at mid-latitudes from SATI observations. *Ann. Geophys.*, *22*(3),

819–828. https://doi.org/10.5194/angeo-22-819-2004

Marsh, D. R., Smith, A. K., Mlynczak, M. G., and Russell, J. M., III. (2006). SABER observations of the OH Meinel airglow variability near the mesopause. *J. Geophys. Res.: Space Phys.*, *111*(A10), A10s05. https://doi.org/10.1029/2005ja011451

Marsh, D. R., Garcia, R. R., Kinnison, D. E., Boville, B. A., Sassi, F., Solomon, S. C., and Matthes, K. (2007). Modeling the whole atmosphere response to solar cycle changes in radiative and geomagnetic forcing. *J. Geophys. Res.: Atmos.*, *112*(D23), D23306. https://doi.org/10.1029/2006jd008306

Melo, S. M. L., Lowe, R. P., and Takahashi, H. (1999). The nocturnal behavior of the hydroxyl airglow at the equatorial and low latitudes as observed by WINDII: Comparison with ground-based measurements. *J. Geophys. Res.: Space Phys.*, *104*(A11), 24657–24665. https://doi.org/10.1029/1999ja900291

Mulligan, F. J., Horgan, D. F., Galligan, J. G., and Griffin, E. M. (1995). Mesopause temperatures and integrated band brightnesses calculated from airglow OH emissions recorded at Maynooth (53.2°N, 6.4°W) during 1993. *J. Atmos.Terr. Phys.*, *57*(13), 1623–1637. https://doi.org/10.1016/0021-9169(94)00133-9

Newman, P. A., Coy, L., Pawson, S., and Lait, L. R. (2016). The anomalous change in the QBO in 2015-2016. *Geophys. Res. Lett.*, *43*(16), 8791–8797. https://doi.org/10.1002/2016gl070373

Pertsev, N., and Perminov, V. (2008). Response of the mesopause airglow to solar activity inferred from measurements at Zvenigorod, Russia. *Ann. Geophys.*, *26*(5), 1049–1056. https://doi.org/10.5194/angeo-26-1049-2008

Pramitha, M., Kumar, K. K., Ratnam, M. V., Praveen, M., and Bhaskara Rao, S. V. (2021). Stratospheric quasi biennial oscillation modulations of migrating diurnal tide in the mesosphere and lower thermosphere over the low and equatorial latitudes. *J. Geophys. Res.: Space Phys.*, *126*(7), e2020JA028970. https://doi.org/10.1029/2020ja028970

Reid, I. M., Spargo, A. J., and Woithe, J. M. (2014). Seasonal variations of the nighttime O(^{1}S) and OH (8-3) airglow intensity at Adelaide, Australia. *J. Geophys. Res.: Atmos.*, *119*(11), 6991–7013. https://doi.org/10.1002/2013jd020906

Russell, J. M. III, Mlynczak, M. G., Gordley, L. L., Tansock, J. J. Jr., and Esplin, R. W. (1999). Overview of the SABER experiment and preliminary calibration results. In *Proceedings Volume 3756, Optical Spectroscopic Techniques and Instrumentation for Atmospheric and Space Research III* (pp. 277-288). Denver, CO, United States: SPIE. https://doi.org/10.1117/12.366382

Shepherd, M. G., Liu, G. P., and Shepherd, G. G. (2006). Mesospheric semiannual oscillation in temperature and nightglow emission. *J. Atmos. Sol. Terr. Phys.*, *68*(3-5), 379–389. https://doi.org/10.1016/j.jastp.2005.02.029

Takahashi, H., Clemesha, B. R., and Batista, P. P. (1995). Predominant semi-annual oscillation of the upper mesospheric airglow intensities and temperatures in the equatorial region. *J. Atmos. Terr. Phys.*, *57*(4), 407–414. https://doi.org/10.1016/0021-9169(94)e0006-9

Tang, C. L., Wu, B., Wei, Y. Y., Qing, C., Dai, C. M., Li, J. Y., and Wei, H. L. (2018). The responses of ozone density to solar activity in the mesopause region and the mutual relationship based on SABER measurements during 2002-2016. *J. Geophys. Res.: Space Phys.*, *123*(4), 3039–3049. https://doi.org/10.1002/2017JA025126

Taylor, M. J., Taori, A. K., Hatch, D. R., Liu, H. L., and Roble, R. G. (2005). Characterization of the semi-annual-oscillation in mesospheric temperatures at low-latitudes. *Adv. Space Res.*, *35*(11), 2037–2043. https://doi.org/10.1016/j.asr.2005.05.111

Teiser, G., and von Savigny, C. (2017). Variability of OH(3-1) and OH(6-2) emission altitude and volume emission rate from 2003 to 2011. *J. Atmos. Sol. Terr. Phys.*, *161*, 28–42. https://doi.org/10.1016/j.jastp.2017.04.010

Teng, C. K. M., Gu, S. Y., Qin, Y. S., and Dou, X. K. (2021). Impact of solar activity on global atmospheric circulation based on SD-WACCM-X simulations from 2002 to 2019. *Atmosphere, 12*(11), 1526. https://doi.org/10.3390/atmos12111526

von Savigny, C., McDade, I. C., Eichmann, K. U., and Burrows, J. P. (2012). On the dependence of the OH* Meinel emission altitude on vibrational level: SCIAMACHY observations and model simulations. *Atmos. Chem. Phys.*, *12*(18), 8813–8828. https://doi.org/10.5194/acp-12-8813-2012

von Savigny, C. (2015). Variability of OH(3-1) emission altitude from 2003 to 2011: Long-term stability and universality of the emission rate-altitude relationship. *J. Atmos. Sol. Terr. Phys.*, *127*, 120–128. https://doi.org/10.1016/j.jastp.2015.02.001

Wallace, J. M. (1973). General circulation of the tropical lower stratosphere. *Rev. Geophys.*, *11*(2), 191–222. https://doi.org/10.1029/RG011i002p00191

Wiens, R. H., and Weill, G. (1973). Diurnal, annual and solar cycle variations of hydroxyl and sodium nightglow intensities in the Europe-Africa sector. *Planet. Space Sci.*, *21*(6), 1011–1027. https://doi.org/10.1016/0032-0633(73)90147-5

Wu, D. L., Hays, P. B., and Skinner, W. R. (1995). A least squares method for spectral analysis of space-time series. *J. Atmos. Sci.*, *52*(20), 3501–3511. https://doi.org/10.1175/1520-0469(1995)052<3501:Alsmfs>2.0.Co;2

Xu, J. Y., Smith, A. K., Liu, H. L., Yuan, W., Wu, Q., Jiang, G. Y., Mlynczak, M. G., Russell, J. M., III, and Franke, S. J. (2009). Seasonal and quasi-biennial variations in the migrating diurnal tide observed by Thermosphere, Ionosphere, Mesosphere, Energetics and Dynamics (TIMED). *J. Geophys. Res.: Atmos.*, *114*(D13), D13107. https://doi.org/10.1029/2008JD011298

Yee, J. H., Crowley, G., Roble, R. G., Skinner, W. R., Burrage, M. D., and Hays, P. B. (1997). Global simulations and observations of O(^{1}S), O_2($^1\Sigma$) and OH mesospheric nightglow emissions. *J. Geophys. Res.: Space Phys.*, *102*(A9), 19949–19968. https://doi.org/10.1029/96ja01833

Zaragoza, G., Taylor, F. W., and López-Puertas, M. (2001). Latitudinal and longitudinal behavior of the mesospheric OH nightglow layer as observed by the Improved Stratospheric and Mesospheric Sounder on UARS. *J. Geophys. Res.: Atmos.*, *106*(D8), 8027–8033. https://doi.org/10.1029/2000jd900633

Zhang, S. P., and Shepherd, G. G. (1999). The influence of the diurnal tide on the O(^{1}S) and OH emission rates observed by WINDII on UARS. *Geophys. Res. Lett.*, *26*(4), 529–532. https://doi.org/10.1029/1999gl900033